

---

# CAETC: Causal Autoencoding and Treatment Conditioning for Counterfactual Estimation over Time

---

Nghia D. Nguyen<sup>1,2</sup> Pablo Robles-Granda<sup>1</sup> Lav R. Varshney<sup>3,4</sup>

## Abstract

Counterfactual estimation over time is important in various applications, such as personalized medicine. However, time-dependent confounding bias in observational data still poses a significant challenge in achieving accurate and efficient estimation. We introduce causal autoencoding and treatment conditioning (CAETC), a novel method for this problem. Built on adversarial representation learning, our method leverages an autoencoding architecture to learn a partially invertible and treatment-invariant representation, where the outcome prediction task is cast as applying a treatment-specific conditioning on the representation. Our design is independent of the underlying sequence model and can be applied to existing architectures such as long short-term memories (LSTMs) or temporal convolution networks (TCNs). We conduct extensive experiments on synthetic, semi-synthetic, and real-world data to demonstrate that CAETC yields significant improvement in counterfactual estimation over existing methods.

## 1. Introduction

Personalized medicine requires knowledge about individualized responses to potential treatments for effective treatment planning (Kent et al., 2018; Feuerriegel et al., 2024). While randomized controlled trials (RCTs) are the gold standard for treatment effect estimation, RCTs in practice are often costly and difficult to implement. Digitization enables more healthcare data to be recorded, especially via electronic health records (EHRs). Combining large data volumes with appropriate modeling can enable accurate estimation of counterfactual outcomes and treatment effects,

forming the basis for individualized decision making in health care (Bareinboim & Pearl, 2016) and other domains.

Modern counterfactual estimation methods integrate frameworks from causal inference and deep learning for counterfactual estimation over time (Lim et al., 2018; Bica et al., 2019; Melnychuk et al., 2022; Bouchattaoui et al., 2024; Wang et al., 2024). However, counterfactual estimation over time is difficult due to time-dependent confounding bias, where covariates that affect treatment choices evolve dynamically and are themselves influenced by prior treatments (Robins et al., 2000). This results in systematic differences in the distribution of confounders between treatment regimes, violating key identification assumptions and complicating the estimation of unbiased causal effects. Conventional time-series models lack the capacity to adjust for this bias, relying on advanced methods to disentangle confounders from treatment assignment.

Learning to balance or disentangle time-dependent confounders is crucial for unbiased counterfactual estimation over time. Modern methods leverage sequence architectures like recurrent neural networks, transformers, or state-space models, with de-confounding mechanisms, like inverse probability of treatment weighting or adversarial balancing, to mitigate time-varying confounding bias, enabling better long-term treatment effect prediction in complex, sequential decision-making settings (Lim et al., 2018; Bica et al., 2019; Melnychuk et al., 2022; Bouchattaoui et al., 2024; Wang et al., 2024). For instance, recurrent marginal structure network (RMSN) (Lim et al., 2018) uses an LSTM architecture with inverse probability of treatment weighting (IPTW). Alternatively, counterfactual recurrent network (CRN) (Bica et al., 2019) uses LSTM architecture with a gradient reversal layer, whereas causal transformer (CT) (Melnychuk et al., 2022) has a transformer architecture with domain confusion loss to learn explicit treatment-invariant representation.

Despite these remarkable advances, several key limitations persist. First, existing methods (CRN, CT) suffer from the loss of covariate information due to adversarial training (Huang et al., 2024). Achieving treatment invariance with an expressive, invertible representation that encodes sufficient information on history for identification of causal ef-

<sup>1</sup>Siebel School of Computing and Data Science, University of Illinois Urbana-Champaign <sup>2</sup>VinUni-Illinois Smart Health Center, VinUniversity <sup>3</sup>AI Innovation Institute, Stony Brook University <sup>4</sup>Department of Electrical and Computer Engineering, University of Illinois Urbana-Champaign. Correspondence to: Nghia Nguyen <nghiadn2@illinois.edu>.

fects remains a challenge. Consequently, models risk learning shortcuts that limit their ability to recover individual-level causal responses or suffer from loss of heterogeneity (Melnychuk et al., 2023). More recent methods, such as causal contrastive predictive coding (CCPC) (Bouchattaoui et al., 2024), tackle the problem implicitly by using the InfoMax principle to encourage representation invertibility. Conversely, Mamba-CDSP (Wang et al., 2024) uses an architecture-specific loss to decorrelate history with planned treatment to circumvent adversarial training. Second, existing methods put little emphasis on modeling the interaction between the planned treatment and the balanced representation to decode future outcomes. While the representation balancing stage yields a theoretically valid representation, the interaction between the representation and planned treatment directly affects the future outcome prediction (see Fig. 2A). By making this interaction explicit, we intuitively and simultaneously encourage representation invertibility and predict future outcomes without excessive architecture changes or complex training procedures.

Inspired by these recent methods and their constraints, we present an architecture-agnostic method called *causal autoencoding and treatment conditioning* (CAETC) for counterfactual estimation over time. Our methodological contributions are the following:

- We design a model-agnostic method for counterfactual estimation over time that encourages a partially invertible representation via autoencoding and predicts future outcomes via treatment conditioning. We further encourage the conditioning layer to learn a treatment-specific transformation to improve counterfactual estimation performance. We apply the proposed design on long-short term memory (LSTM) and temporal convolution network (TCN).
- We propose an entropy maximization adversarial game that yields theoretically balanced representation across all treatment regimes. The adversarial game is equivalent to minimizing a generalized Jensen-Shannon divergence between treatment-conditional representation distributions. We further demonstrate that under certain assumptions and distributional conditions, the outcome estimation error is bounded by the aforementioned Jensen-Shannon divergence term.
- We empirically validate CAETC on synthetic, semi-synthetic, and real-world datasets to demonstrate that our method achieves strong improvement over existing counterfactual estimation baselines.

## 2. Related Works

Counterfactual estimation has received great attention in both static and temporal settings.

Here, we describe prior methods in the temporal domain.

### 2.1. Counterfactual estimation over time

Methods that control for time-dependent confounding were originally developed in epidemiology for longitudinal studies, such as the structural nested model (SNM) (Robins, 1994) and marginal structural model (MSM) (Robins et al., 2000). However, these methods have traditionally been implemented using simple parametric estimators with limited capacity to deal with complex, high-dimensional data. RMSN improves over MSM by incorporating LSTM to handle nonlinearities in the data. However, RMSN still relies on IPTW and suffers from the same problems, such as high variance. Alternatively, G-Net (Li et al., 2021) adapts g-computation (Robins, 1986; 1987) to sequence model. A class of recent methods, such as CRN and CT (Bica et al., 2019; Melnychuk et al., 2022), uses domain adversarial training to learn a treatment-invariant representation, removing the systematic differences between treatment regimes. Further progress has been made toward different approaches to handle time-dependent confounding, such as adapting ODE discovery to treatment effect estimation (Kacprzyk et al., 2023).

### 2.2. Learning treatment-invariant representation

Recent approaches adopt adversarial treatment-invariant representation learning (Bica et al., 2019; Melnychuk et al., 2022; Bouchattaoui et al., 2024) as a foundational building block to balance between treatment groups. More specifically, CRN (Bica et al., 2019) uses a gradient reversal layer (GRL) (Ganin et al., 2016) between an LSTM representation network and a treatment balancing head. The treatment balancing head is optimized to predict the treatment domain from the representation, whereas the GRL encourages a treatment-invariant representation, forming an adversarial game. Similarly, CT (Melnychuk et al., 2022) replaces the LSTM backbone with a combination of three transformer sub-networks to capture long-range dependencies and proposes an adversarial game based on the domain confusion loss. However, an empirical study by Huang et al. (2024) demonstrates that adversarial training results in a significant loss of covariate information, which affects the outcome prediction performance of CRN and CT. Representation invertibility is used as a theoretical tool to ensure a valid representation (Shalit et al., 2017; Johansson et al., 2022; Melnychuk et al., 2023), which can help improve counterfactual estimation performance. CCPC (Bouchattaoui et al., 2024) implicitly encourages reconstructable representation by maximizing mutual information between the input and representation following the InfoMax principle. Alternatively, Mamba-CDSP (Wang et al., 2024) proposes an architecture-specific decorrelation loss to avoid the over-balancing problem of adversarial training. How-

ever, instead of matching the treatment conditional distribution, Mamba-CDSP is only equivalent to first-order moment matching of treatment regimes.

### 3. Problem Formulation

#### 3.1. Outcome forecasting

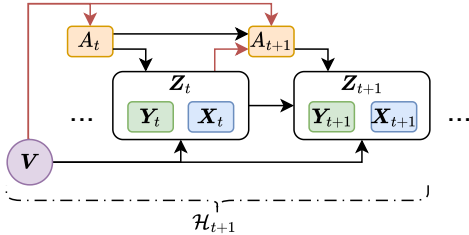


Figure 1. Causal graph for time-dependent confounding over  $\mathcal{H}_t$ .

Our method is designed in the context of the potential outcome framework (Rubin, 2005). Further details on assumptions for causal identification are in Section A. Consider a longitudinal dataset  $\mathcal{D} = \left\{ \{A_{i,t}, \mathbf{Y}_{i,t}, \mathbf{X}_{i,t}\}_{t=1}^T, \mathbf{V}_i \right\}_{i=1}^N$  of  $N$  units and  $T$  time steps with *categorical treatments*  $A_{i,t}$ , vector of *continuous outcomes of interest*  $\mathbf{Y}_{i,t}$ , vector of *continuous time-varying covariates*  $\mathbf{X}_{i,t}$ , and vector of *static covariates*  $\mathbf{V}_i$ . Note that  $\mathbf{Y}_{i,t}$  and  $\mathbf{X}_{i,t}$  are disjoint covariates. Let  $\mathbf{Z}_{i,t} = [\mathbf{X}_{i,t}, \mathbf{Y}_{i,t}]$  be the vector of all considered time-varying covariates. Since  $\mathbf{X}_{i,t}$  may not be present for every dataset  $\mathcal{D}$ ,  $\mathbf{Z}_{i,t}$  is simply  $\mathbf{Y}_{i,t}$  in that case. The history of a unit  $i$  up to time  $T_0$  is defined as  $\mathcal{H}_{i,T_0} = \left\{ \{A_{i,t}, \mathbf{Z}_{i,t}\}_{t=1}^{T_0}, \mathbf{V}_i \right\}$ . The treatment  $A_{i,t}$  affects the time-varying covariates  $\mathbf{Z}_{i,t}$ .<sup>1</sup> For simplicity, we omit the unit index  $i$  in the remainder of this article.

Consider the discrete treatment  $A_t \in \{a^{(1)}, \dots, a^{(K)}\}$  with  $K$  possible values and denote the potential outcome under treatment  $a^{(k)}$  as  $\mathbf{Y}_t[a^{(k)}]$ . Let the sequence of treatments from time  $t+1$  to time  $t+\tau$  as  $A_{t+1:t+\tau}$ . The task of interest is to estimate or forecast the outcome of the next  $\tau$  time steps (prediction horizons) given the history up to time  $T_0$  and the non-random sequence of treatment  $a_{T_0+1:T_0+\tau}$ :

$$\mathbb{E}[\mathbf{Y}_{T_0+\tau}[a_{T_0+1:T_0+\tau}] \mid \mathcal{H}_{T_0}]. \quad (1)$$

Practically, using a neural network, the history  $\mathcal{H}_t$  can be encoded into a latent space by a *representation network*  $\Phi$  before being decoded into estimated outcomes by an *outcome head*  $F_Y$ , similar to prior works (Shalit et al., 2017; Bica et al., 2019; Melnychuk et al., 2022; Bouchattaoui

<sup>1</sup>In several works, the treatment  $A_{i,t-1}$  is denoted to affect the covariates  $\mathbf{Z}_{i,t}$ . We depart from this notation to ensure the history  $\mathcal{H}_{i,t}$  has the same number of time steps for both the treatment  $A$  and covariates  $\mathbf{Z}$ . This change helps simplify the notation in several places while also easing implementation.

et al., 2024). Using the autoregressive decoding strategy, the estimation quantity can be expressed as:

$$F^Y(\Phi(\mathcal{H}_t), A_{t+1}) \approx \mathbb{E}[\mathbf{Y}_{t+1} \mid \Phi(\mathcal{H}_t), A_{t+1}]. \quad (2)$$

The existence of backdoor paths from static covariates  $\mathbf{V}$  and current time-varying covariates  $\mathbf{Z}_t$  to future treatment  $A_{t+1}$ , and the fact that current treatment  $A_t$  also affects current time-varying covariates  $\mathbf{Z}_t$  creates the time-dependent confounding. The confounding paths are shown in Fig. 1 in red. Under time-dependent confounding, the estimation of future outcomes is biased (Robins & Hernán, 2008).

## 4. Method

### 4.1. Architecture overview

Similarly to prior works, we parametrize the representation layer  $\Phi$  by a sequential network such as LSTM (CRN) or transformer (CT). After the representation layer  $\Phi$ , we make an intuitive but important distinction in the architecture. In prior works, the learned representation is then forwarded to the respective treatment balancer  $F^B$ , or is concatenated with the next planned treatment  $A_{t+1}$  to decode the next outcome  $\mathbf{Y}_{t+1}$ , as in Fig. 2A. In this case, if  $\Phi(\mathcal{H}_t)$  is high-dimensional, then the influence of  $A_{t+1}$  is significantly reduced (Shalit et al., 2017).

Instead of the treatment  $A_{t+1}$  being concatenated with  $\Phi(\mathcal{H}_t)$  at the outcome decoder  $F^Y$ , we consider the treatment as conditioning information that transforms the representation at the  $F^C$  layer, as in Fig. 2D. By explicitly modeling the treatment as conditioning information, more complex  $F^C$  can be designed to modulate the representation while also enabling more flexible interactions that serve as building blocks for the rest of our method. Details on  $F^C$  are deferred to Section 4.3.

### 4.2. Input autoencoding

We start with a base autoencoding network to satisfy the representation invertibility as in Fig. 2B. At time step  $T_0$ , we encourage the decoding of current covariates  $\{A_{T_0}, \mathbf{Z}_{T_0}\}$ . Let  $F^H$  be the time step decoding head, which includes three sub-heads: the *treatment decoding head*  $F^A$ , the *outcome of interest decoding head*  $F^Y$ , and the *time-varying covariate decoding head*  $F^X$  if  $\mathbf{X}_t$  exists in the dataset. Note that while we encourage the decoding of the current time step  $T_0$  for simplicity and efficiency, more decoding heads  $F^H$  can be added to decode the last  $\nu$  time steps. However, existing architectures for sequence have built-in mechanisms to selectively remove irrelevant information from the history, i.e., the forget gate in LSTM or the attention in transformer. Therefore, forcing decoding of many past inputs requires the network to remember

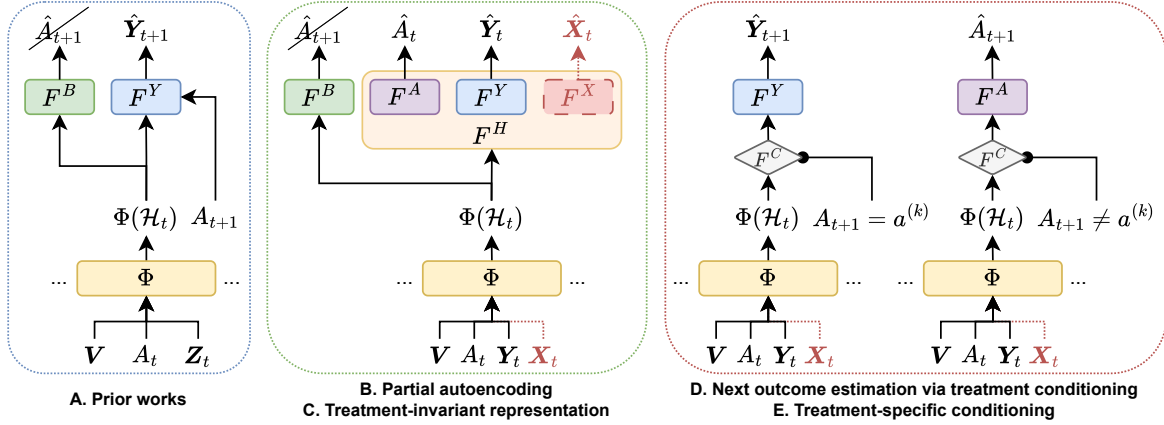


Figure 2. **A.** Prior works concatenate the representation  $\Phi(\mathcal{H}_t)$  with treatment  $A_{t+1}$  to predict next outcomes at  $F^Y$ . We make a distinction to model treatment  $A_{t+1}$  as a transformation on the representation before being forwarded to respective heads. **B.** The history  $\mathcal{H}_t$  is encoded into representation  $\Phi(\mathcal{H}_t)$  before being forwarded to respective heads for decoding. The treatment, outcome, and time-varying covariates estimators  $F^A$ ,  $F^Y$  and  $F^X$  reconstruct  $A_t$ ,  $Y_t$  and  $X_t$ . **C.** Simultaneously, balancing is applied to  $\Phi(\mathcal{H}_t)$  by maximizing the entropy of the treatment balancer  $F^B$ . **D.**  $A_{t+1}$ -specific transformation is applied to the  $\Phi(\mathcal{H}_t)$  before being decoded to the next outcomes by  $F^Y$ . **E.** The conditioning layer  $F^C$  is encouraged to learn treatment-specific transformations of  $\Phi(\mathcal{H}_t)$ .

those steps, which impairs the powerful learning ability of these mechanisms and can negatively impact performance (MacKay et al., 2018).

We define the reconstruction loss for categorical treatments  $A_t$  as the cross-entropy, and for continuous outcomes of interest  $Y_t$  and continuous time-varying covariates  $X$  as the mean squared error. For  $\mathcal{H}_t, A_t, Y_t, X_t, \sim \mathcal{D}$ , we have:

$$\mathcal{L}_t^{RA}(\theta_{F^A}, \theta_\Phi) = - \sum_{j=1}^K \mathbb{I}_{[A_t=a^{(j)}]} \log F_j^A(\Phi(\mathcal{H}_t)) \quad (3)$$

$$\mathcal{L}_t^{RY}(\theta_{F^Y}, \theta_\Phi) = \left\| F^Y(\Phi(\mathcal{H}_t)) - Y_t \right\|_2^2 \quad (4)$$

$$\mathcal{L}_t^{RX}(\theta_{F^X}, \theta_\Phi) = \left\| F^X(\Phi(\mathcal{H}_t)) - X_t \right\|_2^2 \quad (5)$$

where  $\mathbb{I}_C$  is the indicator function for condition C.  $\theta_{F^A}, \theta_{F^Y}, \theta_{F^X}, \theta_\Phi$  are the parameters of  $F^A, F^Y, F^X$ , and  $\Phi$ , accordingly.

The total reconstruction loss is then simply a combination of the above objectives with hyperparameters  $\delta^A$  and  $\delta^X$ . If  $X_t$  is not present in the dataset, then  $\delta^X = 0$ .

$$\begin{aligned} \mathcal{L}_t^R(\theta_{F^A}, \theta_{F^Y}, \theta_{F^X}, \theta_\Phi) &= \mathcal{L}_t^{RY}(\theta_{F^Y}, \theta_\Phi) \\ &+ \delta^A \mathcal{L}_t^{RA}(\theta_{F^A}, \theta_\Phi) \\ &+ \delta^X \mathcal{L}_t^{RX}(\theta_{F^X}, \theta_\Phi). \end{aligned} \quad (6)$$

Prior empirical work by Huang et al. (2024) demonstrates that adversarial training (introduced in Section 4.4) is unstable and may cause the model to lose covariate information. Hence, the model risks violating representation invertibility (Shalit et al., 2017; Zhang et al., 2020; Johans-

son et al., 2022) and suffers loss of heterogeneity (Melnichuk et al., 2023). Despite being an important property to ensure causal identification, representation invertibility, in the context of longitudinal data, has rarely been enforced in practice (CRN - Bica et al. (2019); CT - Melnychuk et al. (2022)) or only been enforced implicitly (CCPC - Bouchattaoui et al. (2024)). Our design starts from explicit partial invertibility as a foundational building block instead.

### 4.3. Outcomes prediction via treatment conditioning

The task of interest is predicting the outcome for the next time step, which can be cast as applying a treatment-specific transformation on the representation  $\Phi(\mathcal{H}_t)$  that corresponds to the future outcomes. This conditioning mechanism may be considered as an inductive bias, i.e., the changes in  $Z_{t+1}$  are caused by applying  $A_{t+1}$ .

More specifically, we apply an element-wise affine transformation to the representation, also known as the feature-wise linear modulation (FiLM) (Perez et al., 2018). For each treatment  $A_{t+1} = a^{(i)}$ , FiLM learns a scaling vector  $\xi^{(i)} = R^\xi(a^{(i)})$  and bias vector  $\beta^{(i)} = R^\beta(a^{(i)})$ , where  $R^\xi, R^\beta$  are the generators that produce the corresponding vectors. The conditioning layer  $F^C$  can then be defined as:

$$F^C(\Phi(\mathcal{H}_t), a^{(i)}) = \Phi(\mathcal{H}_t) \odot \xi^{(i)} \oplus \beta^{(i)} \quad (7)$$

where  $\odot$  and  $\oplus$  are element-wise multiplication and addition, respectively. Implementation-wise,  $R^\xi$  and  $R^\beta$  can be parameterized by a bag of embeddings for categorical treatment or a linear projection for continuous treatment.

Reusing the outcome regressor  $F^Y$ , we define the next outcome prediction loss for  $\mathcal{H}_t, A_{t+1}, Y_{t+1} \sim \mathcal{D}$  as:

$$\mathcal{L}_t^Y(\theta_{F^A}, \theta_{F^C}, \theta_\Phi) = \left\| F^Y(F^C(\Phi(\mathcal{H}_t), A_{t+1})) - \mathbf{Y}_{t+1} \right\|_2^2 \quad (8)$$

Prior works combine the treatment  $A_{t+1}$  with the representation  $\Phi(\mathcal{H}_t)$  via concatenation (Bica et al., 2019; Melnychuk et al., 2022; Bouchattaoui et al., 2024). After the next linear layer, this combination can be considered FiLM’s special case, which is a learnable bias vector. However, this prior approach is limited in the expressiveness of the conditioning mechanism. Note that while we use an efficient FiLM mechanism, a more complex  $F^C$  can be used.

#### 4.4. Treatment-invariant representation learning

Leveraging adversarial domain adaptation, recent methods learn a treatment-invariant representation  $\Phi(\mathcal{H}_t)$ , breaking the association of history  $\mathcal{H}_t$  and planned treatment  $A_{t+1}$ . Let  $P_{(j)}^\Phi$  be the distribution of  $\Phi(\mathcal{H}_t)$  conditioned on a specific treatment  $A_{t+1} = a^{(j)}$  for a fixed time step  $t$ , then recent methods aim to satisfy:

$$P_{(1)}^\Phi = P_{(2)}^\Phi = \dots = P_{(K)}^\Phi. \quad (9)$$

This aspect has been thoroughly explored in the literature. Let  $P_{(j)}^A$  be the marginal distribution of  $A_{t+1} = a^{(j)}$  for a fixed time step  $t$ , the simplified optimization objective for each method is equivalent to:

$$\min_{\Phi} \sum_{j=1}^K \frac{1}{K} \text{KL} \left( P_{(j)}^\Phi \parallel \frac{1}{K} \sum_{k=1}^K P_{(k)}^\Phi \right) \quad (10)$$

CRN (Bica et al., 2019, Appendix D)

$$\min_{\Phi} \sum_{j=1}^K \frac{1}{K} \text{KL} \left( \sum_{k=1}^K P_{(k)}^A P_{(k)}^\Phi \parallel P_{(j)}^\Phi \right) \quad (11)$$

CT (Melnychuk et al., 2022, Appendix F)

$$\min_{\Phi} \sum_{j=1}^K P_{(j)}^A \text{KL} \left( P_{(j)}^\Phi \parallel \sum_{k=1}^K P_{(k)}^A P_{(k)}^\Phi \right) + D \quad (12)$$

CCPC (Bouchattaoui et al., 2024, Appendix G.6)

where (10) is equivalent to minimizing a multi-distribution Jensen-Shannon divergence with equal weights and (12) with weighting factors  $P_{(1)}^A, \dots, P_{(K)}^A$  (Lin, 1991) plus an additional expected divergence term  $D$ . The minima for (10), (11), and (12) satisfy (9).

**Adversarial entropy maximization.** Similar to existing works, we aim to learn a representation that satisfies (9). Consider the *balancing head*  $F^B$ , define the treatment classification loss as the cross-entropy for  $\mathcal{H}_t, A_{t+1} \sim \mathcal{D}$ :

$$\mathcal{L}_t^B(\theta_{F^B}) = - \sum_{j=1}^K \mathbb{I}_{[A_{t+1}=a^{(j)}]} \log F_j^B(\Phi(\mathcal{H}_t)). \quad (13)$$

While the balancing head  $F^B$  predicts the confounded planned treatment  $A_{t+1}$ , the representation  $\Phi(\mathcal{H}_t)$  confuses the balancing head by removing such information. To learn a treatment-invariant representation, we propose to maximize the prediction entropy of  $F^B$  for  $\mathcal{H}_t \sim \mathcal{D}$ :

$$\mathcal{L}_t^E(\theta_\Phi) = \sum_{j=1}^K F_j^B(\Phi(\mathcal{H}_t)) \log F_j^B(\Phi(\mathcal{H}_t)). \quad (14)$$

Minimizing  $\mathcal{L}_t^E$  is equivalent to maximizing the prediction entropy. For a fixed time step  $t$ , let  $\mathbf{H} = \mathcal{H}_t$ , we define the adversarial game as:

$$\begin{aligned} & \arg \min_{F^B} - \sum_{j=1}^K \mathbb{E}_{\Phi(\mathbf{H})|A=a^{(j)}} \left[ \log F_j^B(\Phi(\mathbf{H})) \right] P_{(j)}^A \\ & \arg \max_{\Phi} - \sum_{j=1}^K \mathbb{E}_{\Phi(\mathbf{H})} \left[ F_j^B(\Phi(\mathbf{H})) \log F_j^B(\Phi(\mathbf{H})) \right] \\ & \text{subject to } \sum_{j=1}^K F_j^B(\Phi(\mathbf{H})) = 1. \end{aligned} \quad (15)$$

Next, we show that the equilibrium of (15) satisfies (9). In other words, the representation is treatment-invariant.

**Theorem 4.1.** *For a fixed  $t$ , there exists a pair  $\Phi$  and  $F^B$  that satisfies the equilibrium in (15). The equilibrium holds if and only if  $\Phi$  satisfies (9).*

We also obtained the simplified optimization objective for Eq. (15) as:

$$\min_{\Phi} \sum_{j=1}^K P_{(j)}^A \text{KL} \left( P_{(j)}^\Phi \parallel \sum_{k=1}^K P_{(k)}^A P_{(k)}^\Phi \right). \quad (16)$$

This is similar to the objective of CCPC in Eq. (12) but with a parsimonious and efficient implementation as entropy maximization instead of minimizing the CLUB (Cheng et al., 2020) mutual information upper bound.

Ideally, achieving the equilibrium condition of (9) and satisfying representation invertibility results in a neural network with low estimation error for counterfactual outcomes. However, achieving the equilibrium of the adversarial game can be difficult in practice.

**Bound on prediction error.** Considering binary treatment  $A \in \{0, 1\}$ , we can further show that the prediction error, under some assumptions, is bounded by the generalized Jensen-Shannon divergence between distributions inspired by the results from Shalit et al. (2017). Let  $G^Y = F^Y \circ F^C$ . The expected factual, counterfactual, treated, and control losses for the loss function  $\mathcal{L}$  are defined as:

$$\epsilon^F(G^Y, \Phi) = \mathbb{E}_{\mathbf{H}, \mathbf{Y}, A} \left[ \mathcal{L}(G^Y(\Phi(\mathbf{H}), A), \mathbf{Y}[A]) \right] \quad (17)$$

$$\epsilon^{\text{CF}}(G^Y, \Phi) = \mathbb{E}_{\mathbf{H}, \mathbf{Y}, A} \left[ \mathcal{L}(G^Y(\Phi(\mathbf{H}), 1 - A), \mathbf{Y}[1 - A]) \right] \quad (18)$$

$$\epsilon_{(1)}^F(G^Y, \Phi) = \mathbb{E}_{\mathbf{H}, \mathbf{Y} | A=1} \left[ \mathcal{L}(G^Y(\Phi(\mathbf{H}), 1), \mathbf{Y}[1]) \right] \quad (19)$$

$$\epsilon_{(0)}^F(G^Y, \Phi) = \mathbb{E}_{\mathbf{H}, \mathbf{Y} | A=0} \left[ \mathcal{L}(G^Y(\Phi(\mathbf{H}), 0), \mathbf{Y}[0]) \right]. \quad (20)$$

**Theorem 4.2.** Let  $\Phi$  be an invertible representation function and  $G^Y$  be a hypothesis. Let  $S = \sup_{\mathbf{H}, A} \left| \mathbb{E}_{\mathbf{Y} | \mathbf{H}=\mathbf{h}, A=a} \left[ \mathcal{L}(G^Y(\Phi(\mathbf{h}), a), \mathbf{Y}[a]) \right] \right|$ . Consider the weights  $\pi^{(0)}, \pi^{(1)} > 0$  where  $\pi^{(0)} + \pi^{(1)} = 1$ , let  $W = 2S / (\sqrt{\pi^{(0)}\pi^{(1)}} + \pi^{(0)}\sqrt{\pi^{(1)}})$ , we then have:

$$\begin{aligned} \epsilon^F(G^Y, \Phi) + \epsilon^{\text{CF}}(G^Y, \Phi) &\leq \epsilon_{(0)}^F(G^Y, \Phi) + \epsilon_{(1)}^F(G^Y, \Phi) \\ &\quad + W \sqrt{\text{JS}_{\pi^{(0)}, \pi^{(1)}}(P_{(0)}^\Phi \| P_{(1)}^\Phi)}. \end{aligned} \quad (21)$$

It can be difficult to bound  $S$  without additional assumptions. The first option is bounded loss functions. Alternatively, if we assume the domain of  $\mathbf{V}$  and  $\mathbf{Z}$  is bounded, then  $S$  is bounded. In many applications, such as health care, we can typically assume naturally bounded distributions (e.g., heart rates, etc.).

#### 4.5. Treatment-specific conditioning

By design, the conditioning layer  $F^C$  should learn a treatment-specific transformation of the representation  $\Phi(\mathcal{H}_t)$ . However, during training, only the observable outcome corresponding to the factual treatment  $A_{t+1} = a^{(k)}$  is optimized. Since the counterfactual outcomes cannot be observed, the conditioning with respect to remaining treatments  $A_{t+1} \neq a^{(k)}$  does not receive any training signal.

However, by leveraging the same strategy for next outcome prediction, we synthetically applied the conditioning on the representation  $\Phi(\mathcal{H}_t)$  for all remaining treatments. Reusing the treatment classifier  $F^A$ , for treatment  $a^{(c)} \neq a^{(k)}$ , we optimize:

$$\begin{aligned} &\mathcal{L}_{t,(c)}^C(\theta_{F^A}, \theta_{F^C}, \theta_\Phi) \\ &= - \sum_{j=1}^K \mathbb{I}_{[a^{(c)}=a^{(j)}]} \log F_j^A(F^C(\Phi(\mathcal{H}_t), a^{(c)})). \end{aligned} \quad (22)$$

The final treatment-conditioning loss is simply the average of cross-entropy over all counterfactual treatments:

$$\mathcal{L}_t^C(\theta_{F^A}, \theta_{F^C}, \theta_\Phi) = \frac{1}{K-1} \sum_{c \neq k} \mathcal{L}_{t,(c)}^C(\theta_{F^A}, \theta_{F^C}, \theta_\Phi). \quad (23)$$

Combining the treatment-conditioning loss  $\mathcal{L}_t^C$  with the next outcome prediction loss  $\mathcal{L}_t^Y$ , for every sample in every time step, all possible configurations of the conditioning layer  $F^C$  are optimized. While the  $\mathcal{L}_t^C$  loss is easier to optimize compared to the  $\mathcal{L}_t^Y$  loss, we observe that the additional training signal helps improve counterfactual estimation. Further, during training, to prevent overfitting to the treatment-conditioning loss, it is beneficial to add label smoothing (Müller et al., 2019), which is equivalent to replacing  $\mathbb{I}_{[a^{(c)}=a^{(j)}]}$  with  $\mathbb{I}_{[a^{(c)}=a^{(j)}]}(1 - \alpha) + \mathbb{I}_{[a^{(c)} \neq a^{(j)}]} \frac{\alpha}{K}$  in (22) for some hyperparameter  $\alpha$ .

#### 4.6. Autoregressive decoding

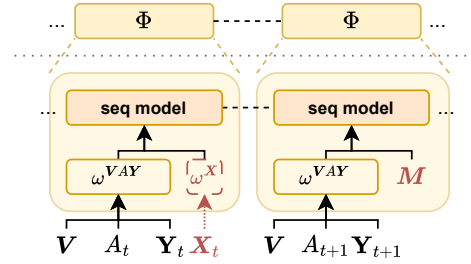


Figure 3. To handle input mismatch of the history  $\mathcal{H}_{T_0} = \{\mathbf{V}, A_t, \mathbf{Y}_t, \mathbf{X}_t\}_{t=1}^{T_0}$  and autoregressively decoded sequences  $\{\mathbf{V}, A_t, \mathbf{Y}_t\}_{t=T_0+1}^{T_0+\tau}$ , we replace the future time-varying covariates  $\{\mathbf{X}\}_{T_0+1}^{T_0+\tau}$  with a learnable vector  $M$ .

At inference time, the predicted outcomes  $\hat{\mathbf{Y}}_{t+1}$  are autoregressively reused to predict the next outcomes. However, if the dataset includes time-varying covariates  $\mathbf{X}_t$ , the network has a mismatched input dimension for future time steps as  $\mathbf{X}_{t+1}$  is not available. For certain types of data, a straightforward solution is also learning to decode  $\mathbf{X}_{t+1}$ .

However, one of the potential problems with decoding  $\mathbf{X}_t$  is that it can be difficult for many scenarios. Forcing the neural network to decode  $\mathbf{X}_{t+1}$  in those cases may waste capacity on a less useful task. Existing works handle the problem by either using an encoder-decoder architecture (Lim et al., 2018; Bica et al., 2019; Bouchattaoui et al., 2024) or masking the corresponding attention of the decoder-only transformer (Melnychuk et al., 2022). We introduce a dropout-like model-agnostic approach called temporal cutoff that can be applied to a decoder-only model as an alternative to an encoder-decoder architecture in prior works.

**Temporal cutoff.** For each training data point, during training, all timesteps  $t \geq T_{\text{cut}} \sim \text{Uniform}(1, T)$  are dropped. To represent the value of the dropped timesteps, a learnable missingness vector  $M$  is used. We apply the temporal cutoff to only  $\mathbf{X}$  if it exists. To allow more capacity to represent missingness, we first linearly project  $\mathbf{X}_t \in \mathbb{R}^u$  to a larger dimension using  $\omega^{\mathbf{X}}$  so that  $\omega^{\mathbf{X}}(\mathbf{X}_t) \in \mathbb{R}^v$  where  $v > u$ . For non-cutoff time steps,  $\omega^{\mathbf{X}}(\mathbf{X}_t) \in \mathbb{R}^v$

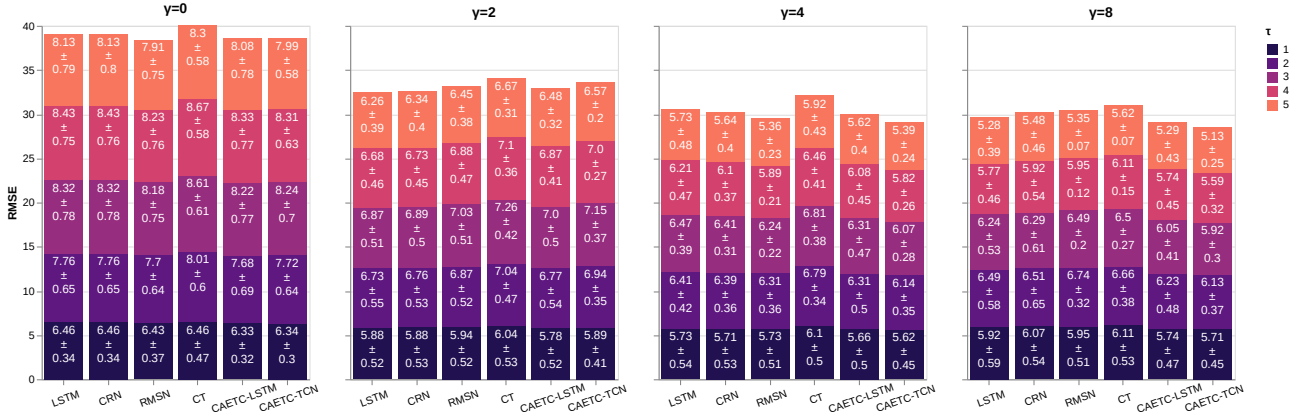


Figure 4. RMSEs for NSCLC fully synthetic data on random trajectories with increasing levels of time-dependent confounding on the training dataset. Each bar represents the RMSE for 5-step-ahead predictions. Lower is better.

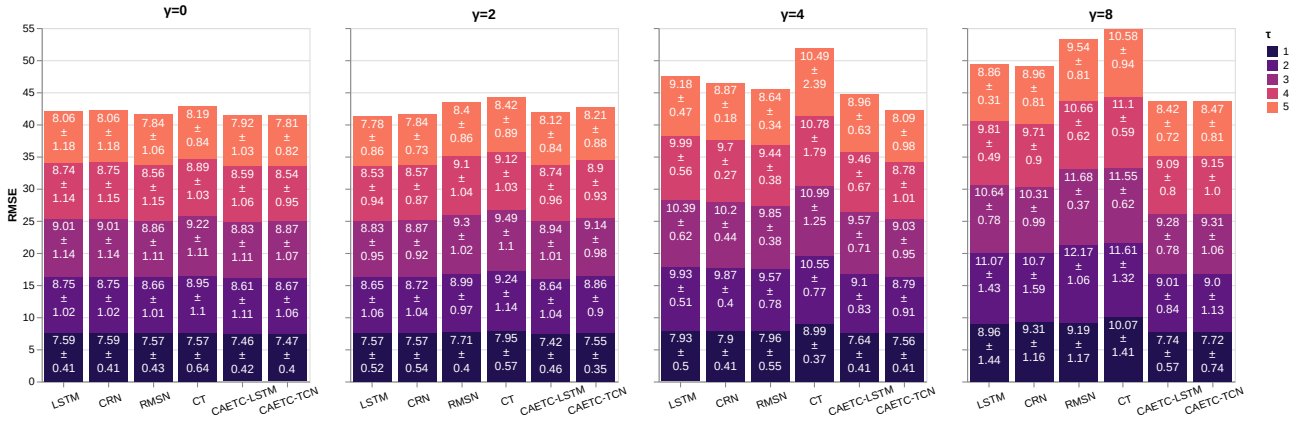


Figure 5. RMSEs for NSCLC fully synthetic data on no-confounding test set ( $\gamma = 0$ ) with increasing levels of time-dependent confounding on the training dataset. Training on  $\gamma = 0$  and testing on  $\gamma = 0$  represents the performance upper bound for each method. Due to time-dependent confounding, training on  $\gamma \neq 0$  and testing on  $\gamma = 0$  is expected to reduce performance. Lower is better.

is used, while for cutoff time steps, the missingness vector  $\mathbf{M} \in \mathbb{R}^v$  is used as the input to the sequence model as in Fig. 3. We also linearly project  $[\mathbf{V}, \mathbf{A}, \mathbf{Y}]$  using  $\omega^{\mathbf{V}, \mathbf{A}, \mathbf{Y}}$  so that  $\omega^{\mathbf{X}}(\mathbf{X}_t)$  do not dominate the input dimension. For simplicity, we let  $\omega^{\mathbf{X}}$  and  $\omega^{\mathbf{V}, \mathbf{A}, \mathbf{Y}}$  projects to the same dimension, i.e.,  $\omega^{\mathbf{V}, \mathbf{A}, \mathbf{Y}}([\mathbf{X}, \mathbf{A}, \mathbf{Y}]) \in \mathbb{R}^v$ .

#### 4.7. Overall training objective

The overall training objective is:

$$\min \delta^E \mathcal{L}_t^B(\theta_{FB}) \quad (24)$$

$$\begin{aligned} \min \mathcal{L}_t^R(\theta_{FA}, \theta_{FY}, \theta_{FX}, \theta_\Phi) + \delta^E \mathcal{L}_t^E(\theta_\Phi) \\ + \mathcal{L}_t^Y(\theta_{FY}, \theta_{FC}, \theta_\Phi) + \delta^A \mathcal{L}_t^C(\theta_{FA}, \theta_{FC}, \theta_\Phi) \end{aligned} \quad (25)$$

with additional hyperparameters  $\delta^E$ . Note that we reuse the hyperparameters  $\delta^A$  from Eq. (6) to reduce hyperparameter search efforts.

## 5. Experiments

### 5.1. Baselines

We evaluate the performance of CAETC against state-of-the-art methods for counterfactual estimation over time, including RMSN (Lim et al., 2018), CRN (Bica et al., 2019), and CT (Melnychuk et al., 2022). Since our method is model-agnostic, we implement two variants of CAETC using LSTM (Hochreiter & Schmidhuber, 1997) and TCN (Bai et al., 2018), which we refer to as CAETC-LSTM and CAETC-TCN, respectively. We also provide a baseline using classical LSTM without balancing, which is equivalent to CRN with no adversarial training. Effective methods for counterfactual estimations should demonstrate performance improvement over classical LSTM.

### 5.2. Datasets

A challenge in evaluating counterfactual estimation methods is the lack of counterfactual outcomes in real-world

Table 1. RMSEs on MIMIC-III semi-synthetic data with counterfactual random trajectories. Lower is better.

	$\tau = 1$	$\tau = 2$	$\tau = 3$	$\tau = 4$	$\tau = 5$	$\tau = 6$	$\tau = 7$	$\tau = 8$	$\tau = 9$	$\tau = 10$	Avg
LSTM	.363±.028	.417±.025	.463±.021	.506±.020	.546±.017	.581±.016	.615±.016	.649±.015	.682±.016	.715±.017	.554
RMSN	.408±.029	.471±.032	.530±.030	.587±.030	.641±.030	.690±.030	.737±.028	.782±.025	.825±.022	.867±.023	.654
CRN	.365±.028	.424±.027	.476±.023	.524±.021	.569±.019	.608±.018	.647±.018	.685±.018	.723±.020	.760±.022	.578
CT	.324±.017	.411±.024	.499±.035	.582±.040	.660±.041	.733±.043	.808±.046	.882±.046	.941±.048	.999±.053	.684
CAETC LSTM	.330±.021	.393±.019	.442±.014	.487±.009	.528±.006	.564±.007	.600±.011	.634±.014	.668±.017	.702±.020	.535
CAETC TCN	.322±.016	.391±.019	.447±.023	.495±.027	.540±.029	.582±.030	.621±.032	.657±.032	.692±.032	.726±.032	.547

datasets. Therefore, we use synthetic data to obtain counterfactual ground truths. To ensure comprehensive evaluation, we benchmark the performance against standard benchmarks used in prior works (Lim et al., 2018; Bica et al., 2019; Melnychuk et al., 2022), including fully synthetic data based on non-small cell lung cancer simulation (Geng et al., 2017) and semi-synthetic data derived from the MIMIC-III dataset (Johnson et al., 2016). We also evaluate CAETC on factual outcomes of real-world data from the MIMIC-III dataset to demonstrate the performance in practical usage. More details are available in the Appendix.

### 5.3. Experiment with synthetic data

The fully synthetic data is built upon the pharmacokinetics-pharmacodynamics model of non-small cell lung cancer (NSCLC) (Geng et al., 2017) under chemotherapy and radiotherapy treatment. Details of the simulation are in Section D. We inject different levels of confounding during simulation, ranging from no confounding  $\gamma = 0$  to strong confounding  $\gamma = 8$ . We set the maximum trajectory length  $T$  to 60 and the prediction horizon  $\tau$  to 5. We trained all methods on the trajectories of 10000 patients with a separate validation set of 1000 patients to select the best hyperparameters. All methods are evaluated under two scenarios: random trajectories and no-confounding. Further details on the test setting are available in the Section D.

**Random trajectories.** At every time step, there are  $K$  possible outcomes. Therefore, at prediction horizon  $\tau$ , there are an exponential  $K^\tau$  outcomes, making simulating every outcome prohibitively expensive. We randomly sample a fixed subset of  $k$  outcomes for evaluation. The setting shares similarities with Melnychuk et al. (2022). We set  $k = 1$  and simulate for 1000 patients, resulting in 1000 test horizons per time step  $t$ .

**No confounding.** As  $\gamma$  can be controlled, we evaluate the model on a non-confounded ( $\gamma = 0$ ) test set to investigate whether the model has learned unbiased estimation. This setting is more difficult than random trajectories, as not only do the prediction horizons not follow the confounded trajectories, but the input history also does not resemble the confounded training set. The setting is similar to Lim et al.

(2018). We use the trajectories of 1000 patients.

**Results.** CAETC-LSTM and CAETC-TCN demonstrate strong performance with increasing time-dependent confounding as in Fig. 4 and Fig. 5. For all methods, training and testing on non-confounded datasets  $\gamma = 0$  in Fig. 5 results in a very small difference in performance, which is desirable. Due to the limited amount of data, similar to real-world scenarios, LSTM and TCN architectures exhibit good performance compared to the transformer architecture. For small confounding, regular LSTM is more stable and demonstrates strong performance compared to counterfactual methods. However, as the confounding factor increases, only CAETC-LSTM and CAETC-TCN exhibit stable counterfactual estimation performance. Prior works (CRN, CT) do not outperform a vanilla LSTM with empirical risk minimization due to covariate information loss (CRN, CT), which is consistent with prior literature (Huang et al., 2024). Our method uses a partial-autoencoding architecture, which is less likely to suffer from the same issues. Furthermore, it can be observed that under the more challenging setting of Fig. 5, CAETC demonstrate strong improvement over existing works.

### 5.4. Experiment with semi-synthetic data

We employ a semi-synthetic dataset generated based on the MIMIC-III (Johnson et al., 2016) intensive care units dataset. Details of the simulation are in Section E. We set the maximum trajectory length  $T$  to 100 and the prediction horizon  $\tau$  to 10. All methods are trained and validated on 2000 and 200 trajectories, respectively. We evaluate the method on random trajectories ( $k = 1$ ) similar to Section 5.3, which includes 200 patients, resulting in 200 test horizons per time step  $t$ .

**Results.** Similar to the synthetic experiment, CAETC-LSTM and CAETC-TCN demonstrate strong improvement across all time steps as in Table 1.

### 5.5. Experiment with real-world data

We further evaluate CAETC on real-world data based on the MIMIC-III dataset (Johnson et al., 2016). However,

for real-world data, counterfactual outcomes are not available. Nonetheless, based on Theorem 4.2, we can expect that a smaller sum of treated and control error indicates a tighter error bound. Therefore, the performance on observable outcomes is still a useful evaluation metric. We set the maximum trajectory length  $T$  to 60 and the prediction horizon  $\tau$  to 5. All methods are trained, validated, and tested on 5000, 500, and 500 trajectories sampled from the dataset, respectively.

**Results.** Similar to previous experiments, CAETC-LSTM and CAETC-TCN achieve strong improvement compared to existing methods as in Table 2.

Table 2. RMSEs on MIMIC-III real-world data. Lower is better.

	$\tau = 1$	$\tau = 2$	$\tau = 3$	$\tau = 4$	$\tau = 5$	Avg
LSTM	6.80±0.02	7.32±0.05	7.61±0.05	7.82±0.05	7.99±0.07	7.51
RMSN	7.29±0.07	7.80±0.07	8.10±0.10	8.33±0.16	8.54±0.21	8.01
CRN	6.81±0.04	7.35±0.05	7.64±0.06	7.86±0.07	8.04±0.10	7.54
CT	6.70±0.04	7.37±0.06	7.71±0.07	7.93±0.07	8.10±0.04	7.56
CAETC LSTM	6.72±0.05	7.27±0.05	7.56±0.06	7.76±0.06	7.91±0.08	7.45
CAETC TCN	6.69±0.06	7.24±0.05	7.53±0.04	7.72±0.03	7.88±0.06	7.41

## 5.6. Ablation

We further examined the performance contribution of each component in CAETC using an LSTM backbone. We consider the following variations: (1) CAETC-LSTM, which achieves state-of-the-art performance; (2) CAETC-LSTM ( $\delta^C = 0$ ), which removes treatment conditioning loss  $\mathcal{L}^C$  (Section 4.5); and (3) CAETC-LSTM ( $\delta^C = \delta^E = 0$ ), which further removes adversarial entropy maximization (Section 4.4). Variation (3) is the basic version, which is only a partial-autoencoding network with treatment conditioning.

**Results.** Observe that each loss contributes to the overall performance. CAETC-LSTM ( $\delta^C = \delta^E = 0$ ) is more biased over the prediction horizon compared to adversarially-trained CAETC-LSTM ( $\delta^C = 0$ ). Due to the partial-autoencoding, CAETC can balance the representation with less covariate information loss.

Table 3. Ablation with the same setting of Fig. 5 with  $\gamma = 8$ .

CAETC LSTM	$\tau = 1$	$\tau = 2$	$\tau = 3$	$\tau = 4$	$\tau = 5$	Avg
Full	7.74±0.57	9.01±0.84	9.28±0.78	9.09±0.8	8.42±0.72	8.71
$\delta^C = 0$	7.75±0.57	9.09±0.86	9.45±0.87	9.37±0.98	8.79±1.04	8.89
$\delta^C = 0$ $\delta^E = 0$	8.01±0.91	9.58±1.31	10.06±1.44	10.05±1.61	9.45±1.49	9.43

## 6. Conclusion

We introduced a novel method for counterfactual estimation over time called causal autoencoding and treatment conditioning. CAETC utilizes a partial autoencoding architecture for representation invertibility and casts outcome prediction as treatment conditioning on the adversarially balanced representation. Extensive empirical experiments show that CAETC improves significantly over baselines.

## Acknowledgements

This work is supported by a VinUni-Illinois Smart Health Center grant (PI: Lav R. Varshney). Nghia D. Nguyen is supported by the Vingroup Science and Technology Scholarship Program for Overseas Study for Master’s and Doctoral Degrees.

## Impact Statement

This paper proposes a novel method for counterfactual estimation over time, which can be beneficial for sequential decision-making systems in domains such as healthcare, economics, or public policy. Improved counterfactual and treatment effect estimation can reduce the bias when learning from observational data. However, misuse or incorrect estimates can result in potentially harmful outcomes, so careful evaluation is required in sensitive applications.

## References

- Bai, S., Kolter, J. Z., and Koltun, V. An empirical evaluation of generic convolutional and recurrent networks for sequence modeling. arXiv:1803.01271, April 2018.
- Bareinboim, E. and Pearl, J. Causal inference and the data-fusion problem. *Proceedings of the National Academy of Sciences*, 113(27):7345–7352, July 2016. doi: 10.1073/pnas.1510507113.
- Bica, I., Alaa, A. M., Jordon, J., and van der Schaar, M. Estimating counterfactual treatment outcomes over time through adversarially balanced representations. In *Proceedings of the International Conference on Learning Representations*, September 2019.
- Bouchattaoui, M. E., Tami, M., Lepetit, B., and Cournède, P.-H. Causal contrastive learning for counterfactual regression over time. In *Advances in Neural Information Processing Systems*, volume 37, pp. 1333–1369, 2024.
- Cheng, P., Hao, W., Dai, S., Liu, J., Gan, Z., and Carin, L. CLUB: A contrastive log-ratio upper bound of mutual information. In *Proceedings of the 37th International Conference on Machine Learning*, pp. 1779–1788, July 2020.
- Detterbeck, F. C. and Gibson, C. J. Turning gray: The natural history of lung cancer over time. *Journal of Thoracic Oncology*, 3(7):781–792, July 2008. doi: 10.1097/JTO.0b013e31817c9230.
- Feuerriegel, S., Frauen, D., Melnychuk, V., Schweisthal, J., Hess, K., Curth, A., Bauer, S., Kilbertus, N., Kohane, I. S., and van der Schaar, M. Causal machine learning for predicting treatment outcomes. *Nature Medicine*, 30(4):958–968, April 2024. doi: 10.1038/s41591-024-02902-1.
- Ganin, Y., Ustinova, E., Ajakan, H., Germain, P., Larochelle, H., Laviolette, F., March, M., and Lempit-sky, V. Domain-adversarial training of neural networks. *Journal of Machine Learning Research*, 17(59):1–35, 2016.
- Geng, C., Paganetti, H., and Grassberger, C. Prediction of treatment response for combined chemo- and radiation therapy for non-small cell lung cancer patients using a bio-mathematical model. *Scientific Reports*, 7(1):13542, October 2017. doi: 10.1038/s41598-017-13646-z.
- Hensman, J., Durrande, N., and Solin, A. Variational Fourier features for Gaussian processes. *Journal of Machine Learning Research*, 18(151):1–52, 2018.
- Hochreiter, S. and Schmidhuber, J. Long short-term memory. *Neural Computation*, 9(8):1735–1780, November 1997. doi: 10.1162/neco.1997.9.8.1735.
- Huang, Q., Meng, C., Cao, D., Huang, B., Chang, Y., and Liu, Y. An empirical examination of balancing strategy for counterfactual estimation on time series. In *Proceedings of the 41st International Conference on Machine Learning*, pp. 20043–20062, June 2024.
- Johansson, F. D., Shalit, U., Kallus, N., and Sontag, D. Generalization bounds and representation learning for estimation of potential outcomes and causal effects. *Journal of Machine Learning Research*, 23(166):1–50, 2022.
- Johnson, A. E. W., Pollard, T. J., Shen, L., Lehman, L.-w. H., Feng, M., Ghassemi, M., Moody, B., Szolovits, P., Anthony Celi, L., and Mark, R. G. MIMIC-III, a freely accessible critical care database. *Scientific Data*, 3(1):160035, May 2016. doi: 10.1038/sdata.2016.35.
- Kacprzyk, K., Holt, S., Berrevoets, J., Qian, Z., and van der Schaar, M. ODE discovery for longitudinal heterogeneous treatment effects inference. In *Proceedings of the 12th International Conference on Learning Representations*, October 2023.
- Kent, D. M., Steyerberg, E., and van Klaveren, D. Personalized evidence based medicine: Predictive approaches to heterogeneous treatment effects. *BMJ*, 363:k4245, December 2018. doi: 10.1136/bmj.k4245.
- Kingma, D. P. and Ba, J. Adam: A method for stochastic optimization. arXiv:1412.6980, January 2017.
- Li, R., Hu, S., Lu, M., Utsumi, Y., Chakraborty, P., Sow, D. M., Madan, P., Li, J., Ghalwash, M., Shahn, Z., and Lehman, L.-w. H. G-Net: A recurrent network approach to G-computation for counterfactual prediction under a dynamic treatment regime. In *Proceedings of Machine Learning for Health*, pp. 282–299, November 2021.
- Lim, B., Alaa, A., and van der Schaar, M. Forecasting treatment responses over time using recurrent marginal structural networks. In *Advances in Neural Information Processing Systems*, volume 31, pp. 7483–7493, 2018.
- Lin, J. Divergence measures based on the Shannon entropy. *IEEE Transactions on Information Theory*, 37(1):145–151, January 1991. doi: 10.1109/18.61115.
- MacKay, M., Vicol, P., Ba, J., and Grosse, R. B. Reversible recurrent neural networks. In *Advances in Neural Information Processing Systems*, volume 31, pp. 9043–9054, 2018.
- Melnychuk, V., Frauen, D., and Feuerriegel, S. Causal transformer for estimating counterfactual outcomes. In *Proceedings of the 39th International Conference on Machine Learning*, pp. 15293–15329, June 2022.

- Melnychuk, V., Frauen, D., and Feuerriegel, S. Bounds on representation-induced confounding bias for treatment effect estimation. In *Proceedings of the 12th International Conference on Learning Representations*, October 2023.
- Müller, R., Kornblith, S., and Hinton, G. E. When does label smoothing help? In *Advances in Neural Information Processing Systems*, volume 32, pp. 4694–4703, 2019.
- Perez, E., Strub, F., de Vries, H., Dumoulin, V., and Courville, A. FiLM: Visual reasoning with a general conditioning layer. In *Proceedings of the Thirty-Second AAAI Conference on Artificial Intelligence and Thirtieth Innovative Applications of Artificial Intelligence Conference and Eighth AAAI Symposium on Educational Advances in Artificial Intelligence*, pp. 3942–3951, February 2018.
- Robins, J. A new approach to causal inference in mortality studies with a sustained exposure period—application to control of the healthy worker survivor effect. *Mathematical Modelling*, 7(9):1393–1512, January 1986. doi: 10.1016/0270-0255(86)90088-6.
- Robins, J. A graphical approach to the identification and estimation of causal parameters in mortality studies with sustained exposure periods. *Journal of Chronic Diseases*, 40:139S–161S, January 1987. doi: 10.1016/S0021-9681(87)80018-8.
- Robins, J. M. Correcting for non-compliance in randomized trials using structural nested mean models. *Communications in Statistics - Theory and Methods*, 23(8):2379–2412, January 1994. doi: 10.1080/03610929408831393.
- Robins, J. M. and Hernán, M. A. Estimation of the causal effects of time-varying exposures. In Fitzmaurice, G., Davidian, M., Verbeke, G., and Molenberghs, G. (eds.), *Longitudinal Data Analysis*. CRC Press, 2008.
- Robins, J. M., Hernán, M. Á., and Brumback, B. Marginal structural models and causal inference in epidemiology. *Epidemiology*, 11(5):550, September 2000.
- Rubin, D. B. Causal inference using potential outcomes: Design, modeling, decisions. *Journal of the American Statistical Association*, 100(469):322–331, March 2005. doi: 10.1198/016214504000001880.
- Shalit, U., Johansson, F. D., and Sontag, D. Estimating individual treatment effect: Generalization bounds and algorithms. In *Proceedings of the 34th International Conference on Machine Learning*, pp. 3076–3085, July 2017.
- Tsybakov, A. B. Lower bounds on the minimax risk. In Tsybakov, A. B. (ed.), *Introduction to Nonparametric Estimation*, pp. 77–135. Springer, New York, NY, 2009. doi: 10.1007/978-0-387-79052-7\_2.
- Wang, H., Li, H., Zou, H., Chi, H., Lan, L., Huang, W., and Yang, W. Effective and efficient time-varying counterfactual prediction with state-space models. In *Proceedings of the 13th International Conference on Learning Representations*, October 2024.
- Wang, S., McDermott, M. B. A., Chauhan, G., Ghassemi, M., Hughes, M. C., and Naumann, T. MIMIC-Extract: A data extraction, preprocessing, and representation pipeline for MIMIC-III. In *Proceedings of the ACM Conference on Health, Inference, and Learning*, pp. 222–235, April 2020. doi: 10.1145/3368555.3384469.
- Williams, R. J. and Zipser, D. A learning algorithm for continually running fully recurrent neural networks. *Neural Computation*, 1(2):270–280, June 1989. doi: 10.1162/neco.1989.1.2.270.
- Zhang, Y., Bellot, A., and Schaar, M. Learning overlapping representations for the estimation of individualized treatment effects. In *Proceedings of the 23rd International Conference on Artificial Intelligence and Statistics*, pp. 1005–1014, June 2020.

## A. Assumptions for causal identification

### A.1. Assumptions

We make the standard assumptions for causal identification (Robins & Hernán, 2008) that are also used in related methods (Bica et al., 2019; Melnychuk et al., 2022; Bouchattaoui et al., 2024).

**Consistency:** If  $A_{\leq t} = a_{\leq t}$  is a sequence of treatments for a given unit, then the potential outcome is equivalent to the observed outcome or  $\mathbf{Y}_t[a_{\leq t}] = \mathbf{Y}_t$ .

**Sequential Positivity:** For every time step, there is a strictly positive probability to observe any treatment level, given a realization of the history. Formally, if  $P(\mathcal{H}_t = h_t) > 0$ , then  $0 < P(A_{t+1} = a_{t+1} | \mathcal{H}_t = h_t)$  for all  $a_{t+1}$ .

**Sequential Ignorability:** For every time step, the treatment assignment  $A_{t+1}$  is independent of potential outcomes, conditioned on the history, or  $\mathbf{Y}_{\geq t+1}[a_{\geq t+1}] \perp A_{t+1} | \mathcal{H}_t$  for all  $a_{\geq t+1}$ .

## B. Proof of Theorem 4.1

The following proofs are adapted from CRN (Bica et al., 2019) and CT (Melnychuk et al., 2022).

**Lemma B.1.** *For a fixed representation network  $\Phi$ , let  $\mathbf{R} = \Phi(\mathbf{H})$ , then the optimal predictor  $F^B$  is:*

$$F_j^{B*}(\mathbf{R}) = \frac{P_{(j)}^A P_{(j)}^\Phi(\mathbf{R})}{\sum_{k=1}^K P_{(k)}^A P_{(k)}^\Phi(\mathbf{R})}. \quad (26)$$

*Proof.* The objective for the predictor  $F^B$  in (15) is:

$$F^{B*} = \arg \min_{F^B} - \sum_{j=1}^K \int \log(F_j^B(\mathbf{r})) P_{(j)}^\Phi(\mathbf{r}) P_{(j)}^A d\mathbf{r} \quad \text{subject to} \quad \sum_{j=1}^K F_j^B(\mathbf{r}) = 1. \quad (27)$$

Minimizing the objective point-wise and applying the Lagrange multiplier:

$$F^{B*} = \arg \min_{F^B} - \sum_{j=1}^K \log(F_j^B(\mathbf{r})) P_{(j)}^\Phi(\mathbf{r}) P_{(j)}^A + \lambda \left( \sum_{j=1}^K F_j^B(\mathbf{r}) - 1 \right). \quad (28)$$

Taking the derivative with respect to  $F_j^B(\mathbf{r})$  and setting to 0:

$$F_j^{B*}(\mathbf{r}) = \frac{P_{(j)}^A P_{(j)}^\Phi(\mathbf{r})}{\lambda}. \quad (29)$$

Solve for  $\lambda$  by the constraint  $\sum_{j=1}^K F_j^B(\mathbf{r}) = 1$  to obtain (26).  $\square$

**Theorem 4.1.** *For a fixed  $t$ , there exists a pair  $\Phi$  and  $F^B$  that satisfies the equilibrium in (15). The equilibrium holds if and only if  $\Phi$  satisfies (9).*

*Proof.* The objective for representation network  $\Phi$  in (15) with  $P^\Phi(\mathbf{r}) = P(\Phi(\mathbf{h}))$  is

$$\Phi^* = \arg \min_{\Phi} \sum_{j=1}^K \int F_j^B(\mathbf{r}) \log(F_j^B(\mathbf{r})) P^\Phi(\mathbf{r}) d\mathbf{r}. \quad (30)$$

Use the optimal predictor obtained from Lemma B.1 and  $P^\Phi(\mathbf{r}) = \sum_{j=1}^K P_{(j)}^A P_{(j)}^\Phi(\mathbf{r})$ :

$$\Phi^* = \arg \min_{\Phi} \sum_{j=1}^K \int \frac{P_{(j)}^A P_{(j)}^\Phi(\mathbf{r})}{\sum_{k=1}^K P_{(k)}^A P_{(k)}^\Phi(\mathbf{r})} \log\left(\frac{P_{(j)}^A P_{(j)}^\Phi(\mathbf{r})}{\sum_{k=1}^K P_{(k)}^A P_{(k)}^\Phi(\mathbf{r})}\right) \sum_{k=1}^K P_{(k)}^A P_{(k)}^\Phi(\mathbf{r}) d\mathbf{r} \quad (31)$$

$$= \arg \min_{\Phi} \sum_{j=1}^K \int P_{(j)}^A P_{(j)}^{\Phi}(\mathbf{r}) \log \frac{P_{(j)}^A P_{(j)}^{\Phi}(\mathbf{r})}{\sum_{k=1}^K P_{(k)}^A P_{(k)}^{\Phi}(\mathbf{r})} d\mathbf{r} \quad (32)$$

$$= \arg \min_{\Phi} \left( \sum_{j=1}^K \int P_{(j)}^A P_{(j)}^{\Phi}(\mathbf{r}) \log \frac{P_{(j)}^{\Phi}(\mathbf{r})}{\sum_{k=1}^K P_{(k)}^A P_{(k)}^{\Phi}(\mathbf{r})} d\mathbf{r} + \sum_{j=1}^K \int P_{(j)}^A P_{(j)}^{\Phi}(\mathbf{r}) \log P_{(j)}^A d\mathbf{r} \right) \quad (33)$$

$$= \arg \min_{\Phi} \left( \sum_{j=1}^K P_{(j)}^A \int P_{(j)}^{\Phi}(\mathbf{r}) \log \frac{P_{(j)}^{\Phi}(\mathbf{r})}{\sum_{k=1}^K P_{(k)}^A P_{(k)}^{\Phi}(\mathbf{r})} d\mathbf{r} + \underbrace{\sum_{j=1}^K P_{(j)}^A \log P_{(j)}^A}_{=C} \underbrace{\int P_{(j)}^{\Phi}(\mathbf{r}) d\mathbf{r}}_{=1} \right) \quad (34)$$

$$= \arg \min_{\Phi} \sum_{j=1}^K P_{(j)}^A \int P_{(j)}^{\Phi}(\mathbf{r}) \log \frac{P_{(j)}^{\Phi}(\mathbf{r})}{\sum_{k=1}^K P_{(k)}^A P_{(k)}^{\Phi}(\mathbf{r})} d\mathbf{r} \quad (35)$$

$$= \arg \min_{\Phi} \sum_{j=1}^K P_{(j)}^A \text{KL} \left( P_{(j)}^{\Phi} \parallel \sum_{k=1}^K P_{(k)}^A P_{(k)}^{\Phi} \right) \quad (36)$$

$$= \arg \min_{\Phi} \text{JS}_{P_{(0)}^A, \dots, P_{(k)}^A} \left( P_{(0)}^{\Phi}, \dots, P_{(k)}^{\Phi} \right) \quad (37)$$

where  $\text{JS}_{P_{(0)}^A, \dots, P_{(k)}^A} \left( P_{(0)}^{\Phi}, \dots, P_{(k)}^{\Phi} \right)$  is the generalized Jensen-Shannon divergence with weight  $P_{(0)}^A, \dots, P_{(k)}^A$  for distributions  $P_{(0)}^{\Phi}, \dots, P_{(k)}^{\Phi}$ . The divergence is non-negative and equals zero if and only if all distributions are identical, which satisfy (9).  $\square$

## C. Proof of Theorem 4.2

We restate Shalit et al. (2017, Lemma A4) with a specific IPM metric, which is the total variation distance between two distributions  $P$  and  $Q$ , denoted as  $\text{TV}(P \parallel Q) = \frac{1}{2} \int |P(\mathbf{x}) - Q(\mathbf{x})| d\mathbf{x}$ .

**Lemma C.1.** *Let  $\Phi : \text{dom}(\mathbf{H}) \rightarrow \text{dom}(\mathbf{R})$  be an invertible representation. Consider the supremum  $S = \sup_{\mathbf{H}, A} \left| \mathbb{E}_{\mathbf{Y} | \mathbf{H}=\mathbf{h}, A=a} [\mathcal{L}(G^Y(\Phi(\mathbf{h}), a), \mathbf{Y}[a])] \right|$ , let  $u = P_{(1)}^A$ , we then have:*

$$\epsilon^{\text{CF}}(G^Y, \Phi) \leq (1-u)\epsilon_{(1)}^{\text{F}}(G^Y, \Phi) + u\epsilon_{(0)}^{\text{F}}(G^Y, \Phi) + 2S \cdot \text{TV} \left( P_{(0)}^{\Phi} \parallel P_{(1)}^{\Phi} \right). \quad (38)$$

*Proof.* Let:

$$\epsilon_{(1)}^{\text{CF}}(G^Y, \Phi) = \mathbb{E}_{\mathbf{H}, \mathbf{Y} | A=1} \left[ \mathcal{L}(G^Y(\Phi(\mathbf{H}), 0), \mathbf{Y}[0]) \right] \quad \text{and} \quad \epsilon_{(0)}^{\text{CF}}(G^Y, \Phi) = \mathbb{E}_{\mathbf{H}, \mathbf{Y} | A=0} \left[ \mathcal{L}(G^Y(\Phi(\mathbf{H}), 1), \mathbf{Y}[1]) \right]. \quad (39)$$

From Shalit et al. (2017, Lemma A3), then

$$\epsilon^{\text{F}}(G^Y, \Phi) = u\epsilon_{(1)}^{\text{F}}(G^Y, \Phi) + (1-u)\epsilon_{(0)}^{\text{F}}(G^Y, \Phi) \quad \text{and} \quad \epsilon^{\text{CF}}(G^Y, \Phi) = (1-u)\epsilon_{(1)}^{\text{CF}}(G^Y, \Phi) + u\epsilon_{(0)}^{\text{CF}}(G^Y, \Phi). \quad (40)$$

Let  $P_{(a)}(\mathbf{h}) = P(\mathbf{h} | A = a)$  and  $\bar{\mathcal{L}}^{G^Y, \Phi}(\mathbf{h}, a) = \mathbb{E}_{\mathbf{Y} | \mathbf{H}=\mathbf{h}, A=a} [\mathcal{L}(G^Y(\Phi(\mathbf{h}), a), \mathbf{Y}[a])]$ . We also have that  $S = \sup_{\mathbf{H}, A} \left| \bar{\mathcal{L}}^{G^Y, \Phi}(\mathbf{h}, a) \right|$ . Then:

$$\epsilon^{\text{CF}}(G^Y, \Phi) - [(1-u)\epsilon_{(1)}^{\text{F}}(G^Y, \Phi) + u\epsilon_{(0)}^{\text{F}}(G^Y, \Phi)] \quad (41)$$

$$= [(1-u)\epsilon_{(1)}^{\text{CF}}(G^Y, \Phi) + u\epsilon_{(0)}^{\text{CF}}(G^Y, \Phi)] - [(1-u)\epsilon_{(1)}^{\text{F}}(G^Y, \Phi) + u\epsilon_{(0)}^{\text{F}}(G^Y, \Phi)] \quad (42)$$

$$= (1-u)[\epsilon_{(1)}^{\text{CF}}(G^Y, \Phi) - \epsilon_{(1)}^{\text{F}}(G^Y, \Phi)] + u[\epsilon_{(0)}^{\text{CF}}(G^Y, \Phi) - \epsilon_{(0)}^{\text{F}}(G^Y, \Phi)] \quad (43)$$

$$= (1-u) \int_{\text{dom}(\mathbf{H})} \bar{\mathcal{L}}^{G^Y, \Phi}(\mathbf{h}, 1) (P_{(0)}(\mathbf{h}) - P_{(1)}(\mathbf{h})) d\mathbf{h} + u \int_{\text{dom}(\mathbf{H})} \bar{\mathcal{L}}^{G^Y, \Phi}(\mathbf{h}, 0) (P_{(1)}(\mathbf{h}) - P_{(0)}(\mathbf{h})) d\mathbf{h} \quad (44)$$

$$\leq (1-u) \sup_{\mathbf{H}} |\bar{\mathcal{L}}^{G^Y, \Phi}(\mathbf{h}, 1)| \int_{\text{dom}(\mathbf{H})} |P_{(0)}(\mathbf{h}) - P_{(1)}(\mathbf{h})| d\mathbf{h} + u \sup_{\mathbf{H}} |\bar{\mathcal{L}}^{G^Y, \Phi}(\mathbf{h}, 0)| \int_{\text{dom}(\mathbf{H})} |P_{(1)}(\mathbf{h}) - P_{(0)}(\mathbf{h})| d\mathbf{h} \quad (45)$$

$$\leq (1-u)S \int_{\text{dom}(\mathbf{H})} |P_{(0)}(\mathbf{h}) - P_{(1)}(\mathbf{h})| d\mathbf{h} + uS \int_{\text{dom}(\mathbf{H})} |P_{(1)}(\mathbf{h}) - P_{(0)}(\mathbf{h})| d\mathbf{h} \quad (46)$$

$$= S \int_{\text{dom}(\mathbf{H})} |P_{(0)}(\mathbf{h}) - P_{(1)}(\mathbf{h})| d\mathbf{h} \quad (47)$$

$$= S \int_{\text{dom}(\mathbf{R})} |P_{(0)}^{\Phi}(\mathbf{r}) - P_{(1)}^{\Phi}(\mathbf{r})| d\mathbf{r} \quad (48)$$

$$= 2S \text{TV} \left( P_{(0)}^{\Phi} \parallel P_{(1)}^{\Phi} \right) \quad (49)$$

where (45) is by the Hölder's inequality and (48) is by the change of variables formula.  $\square$

**Lemma C.2.** Consider the generalized Jensen-Shannon divergence between two distributions  $P$  and  $Q$  with weighting factors  $\pi^P, \pi^Q > 0$  so that  $\pi^P + \pi^Q = 1$ , then:

$$\text{TV}(P \parallel Q) \leq \frac{\sqrt{\text{JS}_{\pi^P, \pi^Q}(P \parallel Q)}}{\sqrt{\pi^P \pi^Q} + \pi^P \sqrt{\pi^Q}}. \quad (50)$$

*Proof.*

$$\text{TV}(P \parallel \pi^P P + \pi^Q Q) = \frac{1}{2} \int |P(x) - \pi^P P(x) - \pi^Q Q(x)| dx \quad (51)$$

$$= \frac{1}{2} \int |\pi^Q P(x) - \pi^Q Q(x)| dx \quad (52)$$

$$= \pi^Q \frac{1}{2} \int |P(x) - Q(x)| dx \quad (53)$$

$$= \pi^Q \text{TV}(P \parallel Q). \quad (54)$$

Similarly, we also have  $\text{TV}(Q \parallel \pi^P P + \pi^Q Q) = \pi^P \text{TV}(P \parallel Q)$ . Then

$$\sqrt{\pi^P \pi^Q} \text{TV}(P \parallel Q) + \pi^P \sqrt{\pi^Q} \text{TV}(P \parallel Q) = \sqrt{\pi^P} \text{TV}(P \parallel \pi^P P + \pi^Q Q) + \sqrt{\pi^Q} \text{TV}(Q \parallel \pi^P P + \pi^Q Q). \quad (55)$$

Using Pinsker's inequality (Tsybakov, 2009),  $\text{TV}(P \parallel Q) \leq \sqrt{\text{KL}(P \parallel Q)}/2$  and the inequality  $a + b \leq \sqrt{2a^2 + 2b^2}$ :

$$\sqrt{\pi^P} \text{TV}(P \parallel \pi^P P + \pi^Q Q) + \sqrt{\pi^Q} \text{TV}(Q \parallel \pi^P P + \pi^Q Q) \quad (56)$$

$$\leq \sqrt{\pi^P} \sqrt{\frac{1}{2} \text{KL}(P \parallel \pi^P P + \pi^Q Q)} + \sqrt{\pi^Q} \sqrt{\frac{1}{2} \text{KL}(Q \parallel \pi^P P + \pi^Q Q)} \quad (57)$$

$$\leq \sqrt{2\pi^P \frac{1}{2} \text{KL}(P \parallel \pi^P P + \pi^Q Q) + 2\pi^Q \frac{1}{2} \text{KL}(Q \parallel \pi^P P + \pi^Q Q)} \quad (58)$$

$$= \sqrt{\pi^P \text{KL}(P \parallel \pi^P P + \pi^Q Q) + \pi^Q \text{KL}(Q \parallel \pi^P P + \pi^Q Q)} \quad (59)$$

$$= \sqrt{\text{JS}_{\pi^P, \pi^Q}(P \parallel Q)}. \quad (60)$$

It follows that

$$\text{TV}(P \parallel Q) \leq \frac{\sqrt{\text{JS}_{\pi^P, \pi^Q}(P \parallel Q)}}{\sqrt{\pi^P \pi^Q} + \pi^P \sqrt{\pi^Q}}. \quad (61)$$

Equality occurs when  $P$  and  $Q$  are identical.  $\square$

**Theorem 4.2.** Let  $\Phi$  be an invertible representation function and  $G^Y$  be a hypothesis. Let  $S = \sup_{\mathbf{H}, A} \left| \mathbb{E}_{\mathbf{Y} | \mathbf{H}=\mathbf{h}, A=a} \left[ (\mathcal{L}(G^Y(\Phi(\mathbf{h}), a), \mathbf{Y}[a])) \right] \right|$ . Consider the weights  $\pi^{(0)}, \pi^{(1)} > 0$  where  $\pi^{(0)} + \pi^{(1)} = 1$ , let  $W = 2S / (\sqrt{\pi^{(0)}\pi^{(1)}} + \pi^{(0)}\sqrt{\pi^{(1)}})$ , we then have:

$$\epsilon^F(G^Y, \Phi) + \epsilon^{\text{CF}}(G^Y, \Phi) \leq \epsilon_{(0)}^F(G^Y, \Phi) + \epsilon_{(1)}^F(G^Y, \Phi) + W \sqrt{\text{JS}_{\pi^{(0)}, \pi^{(1)}}(P_{(0)}^\Phi \| P_{(1)}^\Phi)}. \quad (21)$$

*Proof.* By applying Lemma A3 of Shalit et al. (2017), Lemma C.1, and Lemma C.2:

$$\epsilon^F(G^Y, \Phi) + \epsilon^{\text{CF}}(G^Y, \Phi) \quad (62)$$

$$\leq u\epsilon_{(1)}^F(G^Y, \Phi) + (1-u)\epsilon_{(0)}^F(G^Y, \Phi) + (1-u)\epsilon_{(1)}^F(G^Y, \Phi) + u\epsilon_{(0)}^F(G^Y, \Phi) + 2S \cdot \text{TV}(P_{(0)}^\Phi \| P_{(1)}^\Phi) \quad (63)$$

$$= \epsilon_{(0)}^F(G^Y, \Phi) + \epsilon_{(1)}^F(G^Y, \Phi) + 2S \cdot \text{TV}(P_{(0)}^\Phi \| P_{(1)}^\Phi) \quad (64)$$

$$\leq \epsilon_{(0)}^F(G^Y, \Phi) + \epsilon_{(1)}^F(G^Y, \Phi) + 2S \frac{\sqrt{\text{JS}_{\pi^{(0)}, \pi^{(1)}}(P \| Q)}}{\sqrt{\pi^{(0)}\pi^{(1)}} + \pi^{(0)}\sqrt{\pi^{(1)}}}. \quad (65)$$

□

## D. Non-small Cell Lung Cancer PK-PD Simulation

### D.1. Simulation details

Similar to prior works (Lim et al., 2018; Bica et al., 2019; Melnychuk et al., 2022), we evaluate CAETC on a pharmacokinetics-pharmacodynamics model of non-small cell lung cancer (Geng et al., 2017).

The model simulates the tumor volume over time under chemotherapy and radiotherapy. Parameters in the form of  $\zeta^{\text{param}}$  are either given or sampled from the distribution in Geng et al. (2017). Consider the discrete-time model of volume of the tumor  $Y_t$ , the chemotherapy drug concentration  $C_t$ , and the radiotherapy dose  $D_t$ :

$$Y_{t+1} = \left( \underbrace{1 + \zeta^\rho \log \frac{\zeta^K}{Y_t}}_{\text{tumor growth}} + \underbrace{\epsilon_t}_{\text{noise}} - \underbrace{\zeta^{\beta_C} C_{t+1}}_{\text{chemotherapy}} - \underbrace{(\zeta^\alpha D_{t+1} + \zeta^\beta D_{t+1}^2)}_{\text{radiotherapy}} \right) Y_t \quad (66)$$

where one unit of time is one day. A noise term  $\epsilon_t \sim \text{Normal}(0, 0.01^2)$  is added to account for randomness in tumor growth. The tumor is assumed to be spherical.

The chemotherapy concentration is modeled as an exponential decay with a half-life of one day as  $C_t = \tilde{C}_t + C_{t-1}/2$ . The dosage if used of chemotherapy  $\tilde{C}_t$  and radiotherapy  $D_t$  are 5.0 mg/m<sup>3</sup> of Vinblastine and 2.0 Gy fractions, respectively. Heterogeneous static features  $V$  are generated by augmenting the prior means of  $\zeta^\alpha, \zeta^\beta$ . The patients are divided into three groups  $V \sim \text{Uniform}\{1, 2, 3\}$ . The augmented prior means  $\zeta^{\mu_\alpha}, \zeta^{\mu_{\beta_C}}$  are then defined as:

$$\zeta^{\mu_{\beta_C}} = \begin{cases} 1.1\zeta^{\mu_{\beta_C}} & \text{if } V = 3 \\ \zeta^{\mu_{\beta_C}} & \text{otherwise} \end{cases} \quad \zeta^{\mu_\alpha} = \begin{cases} 1.1\zeta^{\mu_\alpha} & \text{if } V = 1 \\ \zeta^{\mu_\alpha} & \text{otherwise} \end{cases} \quad (67)$$

Time-varying confounding is introduced by modeling treatment assignment as a Bernoulli variable:

$$A_{t+1}^{\text{chemo}}, A_{t+1}^{\text{radio}} \sim \text{Bernoulli} \left( \sigma \left( \frac{\gamma}{\text{diam}(Y_{\max})} \left( \overline{\text{diam}(Y_{>t-15})} - \frac{\text{diam}(Y_{\max})}{2} \right) \right) \right) \quad (68)$$

where  $\sigma$  is the sigmoid function,  $\text{diam}(Y_{\max})$  is the maximum tumor diameter (13 cm),  $\overline{\text{diam}(Y_{>t-15})}$  is the average tumor diameter over the last 15 days. The value of  $\gamma$  directly affects the strength of time-dependent confounding, i.e., the larger the value of  $\gamma$ , the larger the time-dependent confounding.

Each tumor has an initial stage proportional to the value in Detterbeck & Gibson (2008). Given the initial stage, the initial volume  $Y_1$  is correspondingly sampled from the stage distribution as in Geng et al. (2017). For treatment initial value,  $C_1 = \tilde{C}_1 = 0$  mg/m<sup>3</sup> and  $D_1 = 0$  Gy fractions.

Trajectories are measured until one of the following conditions happens: 1) The tumor diameter reaches  $\text{diam}(Y_{\max}) = 13$  cm. 2) Patient recovers with probability  $\exp(-Y_t \zeta^\eta)$  where  $\zeta^\eta$  is the tumor cell density as specified in Geng et al. (2017). 3) Termination after reaching the maximum time step  $T = 60$  days.

## D.2. Experimental details

We generate 10000, 1000, and 1000 patients for training, validation, and testing. For training and testing, we simulate the full factual trajectories. All methods are tested on two settings: random trajectories and no confounding. We set  $\tau = 5$ , i.e., 5-step ahead prediction.

**Random trajectories.** At every time step  $t$ , we evaluate the methods by predicting potential horizons given the history  $\mathcal{H}_t$ . Therefore, for each  $t$ , we need to simulate an exponential of  $K^\tau$  outcomes for a prediction horizon of  $\tau$ , which is prohibitively expensive. We can randomly sample a fixed subset of  $k$  outcomes for evaluation, which includes both factual and counterfactual outcomes. This setting is similar to the setting in Melnychuk et al. (2022). We set  $k = 1$  and simulate 1000 patients, resulting in 1000 test horizons per time step  $t$ . Since  $T = 60$  and  $\tau = 5$ , we obtain 55 steps for history, resulting in  $55 \times 1000 = 55000$  test horizons.

**No confounding.** At every time step  $t$ , we evaluate the methods by predicting factual horizons given the history  $\mathcal{H}_t$ . As the parameter  $\gamma$  can be controlled, we evaluate the model on a non-confounded ( $\gamma = 0$ ) test set. This setting is more difficult than random trajectories. In the random trajectories, the input history resembles the confounded training set distribution, while the test horizons do not. In the no-confounding setting, neither the history nor the test horizon resembles the training set distribution. For this strategy, we would only need to generate the factual outcomes for testing. The setting is similar to Lim et al. (2018). We use the trajectories of 1000 patients.

## E. MIMIC-III Dataset

We generate semi-synthetic data based on the MIMIC-III dataset (Johnson et al., 2016) using a similar protocol to Melnychuk et al. (2022) with some minor modifications to simplify the simulation. Similarly, the real-world data selection also follows Melnychuk et al. (2022). We used the MIMIC-Extract preprocessing pipeline (Wang et al., 2020) to obtain the hourly aggregated data for the intensive care unit (ICU). All continuous time-varying covariates are further processed using forward filling, backward filling, and normalization.

From the hourly data, we extract 25 time-varying covariates  $\mathbf{X}_t$  and 3 static covariates  $\mathbf{V}$  as in Table 4. The static covariates are one-hot encoded into a 44-dimensional feature vector. Patients with less than 20 hours of ICU stay are removed.

### E.1. Semi-synthetic simulation details

The ICU maximum stay is cut off at 100 hours, creating time-varying covariates  $\mathbf{X}_t$  with a maximum time step of  $T = 100$ .

We generate  $N^Y = 2$  outcomes. For an outcome  $m$ , denoted as  $Y_{i,t}^{(m)}$ , the simulation first creates a non-treated outcomes  $\tilde{Y}_{i,t}^{(m)}$ . The non-treated outcome consists of an endogenous dependency by a combination of B-spline and Gaussian process. For every outcome simulated, we randomly sampled a subset of 10 time-varying covariates  $\mathbf{X}_{i,t}^{(m)}$  to be the exogenous dependency. Assuming the outcome  $m$  is affected by a set of treatments  $\mathbf{A}_{i,t}^{(m)}$  with treatment effects  $\mathbf{E}_{i,t}^{(m)}$  (defined later), we then have:

Table 4. Selected time-varying covariates and static covariates from the MIMIC-Extract processed data.

Time-varying covariates
heart rate
red blood cell count
sodium
mean blood pressure
systemic vascular resistance
glucose
chloride urine
glasgow coma scale total
hematocrit
positive end-expiratory pressure set
respiratory rate
prothrombin time pt
cholesterol
hemoglobin
creatinine
blood urea nitrogen
bicarbonate
calcium ionized
partial pressure of carbon dioxide
magnesium
anion gap
phosphorous
venous pvo2
platelets
calcium urine
Static covariates
gender
ethnicity
age

$$\tilde{Y}_{i,t}^{(m)} = \underbrace{u_i^{(m)}}_{\text{initial value}} + \underbrace{\alpha^b b_i(t) + \alpha^g g_i^{(m)}(t)}_{\text{endogenous}} + \underbrace{\alpha^f f^{(m)}(\mathbf{X}_{i,t}^{(m)})}_{\text{exogenous}} + \underbrace{\epsilon_{i,t}^{(m)}}_{\text{noise}} \quad (69)$$

$$Y_{i,t}^{(m)} = \tilde{Y}_{i,t}^{(m)} + \mathbf{E}_{i,t}^{(m)\top} \mathbf{1} \quad (70)$$

where  $\alpha^b$ ,  $\alpha^g$ , and  $\alpha^f$  are weight for each component. Each component is defined as follows. The initial value is defined as  $u_i^{(m)} \sim \text{Uniform}(-0.5, 0.5)$ . The spline  $b(\cdot) \sim \text{Uniform}\{b^{\text{stable}}(\cdot), b^{\text{fast decline}}(\cdot), b^{\text{slow decline}}(\cdot), b^{\text{fast increase}}(\cdot), b^{\text{slow increase}}(\cdot)\}$  is a cubic spline sampled uniformly from a set of five cubic splines representing different global trends. The Gaussian process instance  $g_i^{(m)}(t) \sim \mathcal{GP}(0, \text{Matern}_{\nu=2.5})$  represent smooth local trend. Exogenous dependency is introduced by a non-linear function of the selected covariates, constructed by random Fourier features approximating an RBF kernel  $f^{(m)}(\mathbf{X}_{i,t}^{(m)}) = \phi(\mathbf{X}_{i,t}^{(m)})^\top \mathbf{w}$  as in (Hensman et al., 2018) with  $\mathbf{w} \sim \text{Normal}(0, \sigma_w^2 \mathbf{I})$ . A noise term is added to account for randomness  $\epsilon_{i,t}^{(m)} \sim \text{Normal}(0, 0.05^2)$ .

We generate  $N^A = 3$  treatments. The confounded treatment  $l$ , denoted  $A_{i,t}^{(l)}$  and its treatment effect  $E_{i,t}^{(l)}$ , is generated as:

$$P_{i,t+1}^{(l)} = \sigma \left( \gamma^Y \overline{\mathbf{Y}_{i,>t-w^{(l)}}^{(l)}} + \gamma^X f^{(l)}(\mathbf{X}_{i,t}) \right) \quad (71)$$

$$A_{i,t}^{(l)} \sim \text{Bernoulli}(P_{i,t}^{(l)}) \quad (72)$$

$$E_{i,t}^{(l)} = \sum_{v=0}^{\omega^{(l)}-1} \frac{P_{i,t-v}^{(l)} A_{i,t-v}^{(l)} b}{2^{-v/2}} \quad (73)$$

where  $\gamma^Y$  and  $\gamma^X$  are confounding parameters.  $\overline{\mathbf{Y}_{i,>t-w^{(l)}}^{(l)}}$  is the average outcomes over the last  $w^{(l)}$  hours. Note that  $\mathbf{Y}_{i,t}^{(l)}$  is a subset of treated outcomes that confound with the treatment. Similar to the synthetic outcome, we also sampled a subset of 10 time-varying covariates  $\mathbf{X}_{i,t}^{(l)}$  to be the confounding covariates for each treatment.  $f^{(l)}$  is a non-linear function similar to  $f^{(m)}$ . The treatment assignment  $A^{(l)}$  is modeled as a Bernoulli random variable with probability  $P_{i,t}^{(l)}$ . The treatment effect  $E_{i,t}^{(l)}$  is just the sum of all treatments used within  $\omega^{(l)}$  hours with scaling factor  $b$ . All treatment has maximum effect right after use but decay exponentially with a half-life of 2 hours.

We can observe that each outcome  $Y_{i,t}^{(m)}$  is affected by multiple treatment  $A_{i,t}^{(m)}$  and each treatment  $A_{i,t}^{(l)}$  is confounded with multiple outcomes  $\mathbf{Y}_{i,t}^{(l)}$ , creating a complex dynamic.

## E.2. Semi-synthetic experiment details

We simulate 2000 and 200 patients for training and validation. For training and testing, we simulate the full factual trajectories. For testing, we use the random trajectories strategy similar to Section D.2. We set  $\tau = 10$ , i.e., 10-step ahead prediction. Note that while the semi-synthetic MIMIC-III simulation also has a confounding parameter  $\gamma^Y$  and  $\gamma^X$ , the treatment mechanism is different for different values of  $\gamma^Y$  and  $\gamma^X$ . Therefore, we do not apply the no-confounding setting test to this simulation.

## E.3. Real-world data details

For real-world data, we extract two binary treatments, including `vaso` (vasopressor  $A_t^{\text{vaso}}$ ) and `vent` (mechanical ventilation  $A_t^{\text{vent}}$ ), and two outcomes  $\mathbf{Y}_t$ , including diastolic blood pressure and oxygen saturation. The ICU maximum stay is cut off at 60 hours, creating trajectories with a maximum time step of  $T = 60$ .

## E.4. Real-world experiment details

We select a subset of 5000 and 500 patients for training and validation. At every time step, we evaluate the methods by predicting the factual horizon  $\tau$  given the history  $\mathcal{H}_t$ . We select a different subset of 500 patients for testing. We set  $\tau = 5$ , i.e., 5-step ahead prediction.

## F. Baseline Methods

### F.1. Common structure

To ensure a fair comparison for all methods, we use a common structure including several components similar to Fig. 2A. All methods include a representation function  $\Phi$  and an outcome prediction head  $F^Y$  (Table 5a). For adversarial-based methods like CAETC, CRN, and CT, an additional balancing head  $F^B$  is added (Table 5b).  $F^Y$  and  $F^B$  share the same architectures for all methods, with the only potential difference being the input size for  $F^Y$  and  $F^B$ . All methods are trained with Adam optimizers (Kingma & Ba, 2017) and the teacher forcing technique (Williams & Zipser, 1989). The dimension of  $\Phi(\mathcal{H}_t)$  is referred to as # hidden units in the hyperparameter search table in Section G. # hidden units are selected so that all methods have roughly the same total parameter range.

Table 5

(a) Architecture for $F^Y$	(b) Architecture for $F^B$
<b>Input:</b> $[\Phi(\mathcal{H})_t, A_{t+1}]$ or $\Phi(\mathcal{H})_t$ or $F^C(\Phi(\mathcal{H})_t, A_{t+1})$	<b>Input:</b> $\Phi(\mathcal{H})_t$
Linear Layer	Linear
ELU Activation	ELU
Linear Layer	Linear
	Softmax
<b>Output:</b> $\hat{Y}_{t+1}$ or $\hat{Y}_t$	<b>Output:</b> $\hat{A}_{t+1}$

### F.2. CAETC

**Architecture.** CAETC uses a decoder-only architecture. The representation network  $\Phi$  for CAETC is parametrized by either LSTM cells (Hochreiter & Schmidhuber, 1997) layers or TCN residual blocks (Bai et al., 2018). We refer to both as layers. Since TCN is composed of dilated causal convolutions with an exponential receptive field as a function of depth, TCN requires more layers to cover the entire history. The architecture for  $\Phi$  is in Table 6c. The output dimension for both projection layers is set to # hidden units.

Table 6

(a) Architecture for $\omega^{X,A,Y}$	(b) Architecture for $\omega^X$	(c) Architecture for $\Phi$ (CAETC)
<b>Input:</b> $[V, A_t, Y_t]$	<b>Input:</b> $X_t$	<b>Input:</b> $\mathcal{H}_t$
Linear Layer	Linear Layer	$\omega^{X,A,Y}$ and $\omega^X$
<b>Output:</b> $\omega^{X,A,Y}([V, A_t, Y_t])$	<b>Output:</b> $\omega^X(X_t)$	LSTM (# layers) or TCN (# layers)
		Linear Layer
		ELU Activation
		<b>Output:</b> $\Phi(\mathcal{H})_t$

For CAETC, two additional heads  $F^A$  (Table 7a) and  $F^X$  (Table 7b) and a conditioning layer  $F^C$  (Table 7c) are added.

Table 7

(a) Architecture for $F^A$	(b) Architecture for $F^X$	(c) Architecture for $F^C$
<b>Input:</b> or $\Phi(\mathcal{H})_t$ or $F^C(\Phi(\mathcal{H})_t, A_{t+1})$	<b>Input:</b> $\Phi(\mathcal{H})_t$	<b>Input:</b> $\Phi(\mathcal{H}_t)$ and $a^{(k)}$
Linear Layer	Linear Layer	2x Embedding for $R^\xi$ and $R^\beta$
ELU Activation	ELU Activation	
Linear Layer	Linear Layer	<b>Output:</b> $\Phi(\mathcal{H}_t) \odot \xi^{(k)} \oplus \beta^{(k)}$
Softmax		
<b>Output:</b> $\hat{A}_t$ or $\hat{A}_{t+1}$	<b>Output:</b> $\hat{X}_t$	

**Training.** The training process is in Algorithm 1. We set  $\delta^A = 0.1$ ,  $\delta^X = 0.1$  and  $\delta^B = 0.0001$  for all experiments.

**Algorithm 1** Training algorithm for CAETC

---

**Input:** Dataset  $\mathcal{D} = \left\{ \{A_{i,t}, \mathbf{Y}_{i,t}, \mathbf{X}_{i,t}\}_{t=1}^T, \mathbf{V}_i \right\}_{i=1}^N$ , hyperparameters  $\delta^A, \delta^X, \delta^E$   
**for** epoch  $e_j = 1$  to  $e_{\max}$  **do**  
     Compute loss  $\mathcal{L}(\theta_{FA}, \theta_{FY}, \theta_{FX}, \theta_{FC}, \theta_{\Phi})$   
      $= [\mathcal{L}^{RY}(\theta_{FY}, \theta_{\Phi}) + \mathcal{L}^Y(\theta_{FY}, \theta_{FC}, \theta_{\Phi})] + \delta^A [\mathcal{L}^{RA}(\theta_{FA}, \theta_{\Phi}) + \mathcal{L}^C(\theta_{FA}, \theta_{FC}, \theta_{\Phi})] + \delta^X \mathcal{L}^{RX}(\theta_{FX}, \theta_{\Phi}) + \delta^E \mathcal{L}^E(\theta_{\Phi})$   
     Compute gradient  $\nabla_{\theta_{FA}, \theta_{FY}, \theta_{FX}, \theta_{FC}, \theta_{\Phi}} [\mathcal{L}(\theta_{FA}, \theta_{FY}, \theta_{FX}, \theta_{FC}, \theta_{\Phi})]$   
     Compute loss  $\delta^E \mathcal{L}^B(\theta_{FB})$   
     Compute gradient  $\nabla_{\theta_{FB}} [\delta^E \mathcal{L}^B(\theta_{FB})]$   
     Update parameters  $\theta_{FA}, \theta_{FY}, \theta_{FX}, \theta_{FC}, \theta_{\Phi}$  by gradient  $\nabla_{\theta_{FA}, \theta_{FY}, \theta_{FX}, \theta_{FC}, \theta_{\Phi}} [\mathcal{L}(\theta_{FA}, \theta_{FY}, \theta_{FX}, \theta_{FC}, \theta_{\Phi})]$   
     Update parameters  $\theta_{FB}$  by gradient  $\nabla_{\theta_{FB}} [\delta^E \mathcal{L}^B(\theta_{FB})]$   
**end for**

---

### F.3. RMSN

RMSN requires the estimation of  $P(A_{t+1}|A_t)$  and  $P(A_{t+1}|\mathcal{H}_t)$  for IPTW, each of which is parametrized by an LSTM. They are referred to as the propensity-treatment network and the propensity-history network. RMSN uses an encoder-decoder architecture. The propensity-treatment network and propensity-history network are both composed of a representation function  $\Phi$  and a treatment classification head, for which we reuse the architecture of  $F^B$  (Table 5b). The encoder and decoder are both composed of a representation function  $\Phi$  and an outcome prediction head  $F^Y$  (Table 5a). The architecture of  $\Phi$  is similar for the propensity-treatment network, the propensity-history network, the encoder, and the decoder as in Table 8. In total, RMSN requires four different individual networks for training.

 Table 8. Architecture for  $\Phi$  (RMSN)

<b>Input:</b> $\{A_{t'}\}_{t'=1}^t$ or $\mathcal{H}_t$
LSTM (# layers)
Linear Layer
ELU Activation
<b>Output:</b> $\Phi(\{A_{t'}\}_{t'=1}^t)$ or $\Phi(\mathcal{H}_t)$

### F.4. CRN

CRN uses an encoder-decoder architecture with a gradient reversal layer for adversarial training. Both the encoder and decoder are composed of a representation function  $\Phi$  (Table 9), an outcome prediction head  $F^Y$  (Table 5a), and a treatment balancing head  $F^B$  (Table 5b). CRN requires a hyperparameter for adversarial training, which is similar to our  $\delta^B$ . We set CRN's  $\delta^B = 0.1$ .

 Table 9. Architecture for  $\Phi$  (CRN)

<b>Input:</b> $\mathcal{H}_t$
LSTM (# layers)
Linear Layer
ELU Activation
<b>Output:</b> $\Phi(\mathcal{H}_t)$

### F.5. CT

CT uses a decoder-only architecture and domain confusion loss for adversarial training. The decoder is composed of a representation function  $\Phi$  (Table 10), an outcome prediction head  $F^Y$  (Table 5a), and a treatment balancing head  $F^B$  (Table 5b). CT also requires an exponential moving average (EMA) copy of the decoder. We reuse original hyperparameters in CT for the EMA copy. CT requires a hyperparameter for adversarial training, which is similar to our  $\delta^B$ . We set CT's  $\delta^B = 0.01$ .

 Table 10. Architecture for  $\Phi$  (CT)

<b>Input:</b> $\mathcal{H}_t$
3x Transformers (# layers)
<b>Output:</b> $\Phi(\mathcal{H}_t)$

### F.6. Adversarial weight $\delta^B$

For all methods that use  $\delta^B$ , we perform an exponential increase in the value of  $\delta_e^B$  as a function of the epoch until we reach  $\delta^B$ .

$$\delta_{e_j}^B = \delta^B \left( \frac{2}{1 + \exp(-10 \times e_j / e_{\max})} - 1 \right) \quad (74)$$

## G. Hyperparameter Search

Table 11. Hyperparameter search range for every method & dataset. If multiple components (e.g., encoder & decoder) are in the same cell, the hyperparameter is shared for those components (e.g., encoder and decoder have the same number of layers) for the same run. Otherwise, the hyperparameter is component-specific for the same run. We run a random grid search with 10 combinations for every method for fair comparison. The final results reported are averaged over 3 random seeds.

Method	Components	Hyperparameters	NSCLC range	MIMIC III range (semi-synthetic & real)
LSTM & CRN	Encoder & Decoder	# layers # hidden units Dropout rate	1 16, 32, 48	1,2 32, 48, 64 0.0, 0.1
	Encoder	# epochs Learning rate Batch size	100	150 0.001, 0.0001 64, 128
	Decoder	# epochs Learning rate Batch size	50	100 0.001, 0.0001 512, 1024
RMSN	Propensity <sup>1</sup> & Encoder & Decoder	# layers # hidden units Dropout rate	1 16, 32, 48	1,2 32, 48, 64 0.0, 0.1
	Propensity <sup>1</sup> & Encoder	# epochs Learning rate	100	150 0.001, 0.0001
	Decoder	# epochs Learning rate	50	100 0.001, 0.0001
CT		# layers # hidden units # attention heads Max positional encoding # epochs Dropout rate Learning rate Batch size	1 16, 24, 32 2 15 150	1,2 18, 24, 36 2,3 30 250 0.0, 0.1 0.001, 0.0001 64, 128
CAETC LSTM		# layers # hidden units # epochs Dropout rate Learning rate Batch size	1 16, 32, 48 150	1,2 32, 48, 64 250 0.0, 0.1 0.001, 0.0001 64, 128
CAETC TCN		# layers # hidden units Kernel size Dilation factor # epochs Dropout rate Learning rate Batch size	3,4, 5 16, 24, 32 150	4,5, 6 24, 32, 40 3, 5 2 250 0.0, 0.1 0.001, 0.0001 64, 128

<sup>1</sup> Both the propensity-treatment & propensity-history networks are referred to as “propensity”.